

1 **Genesis of Diamond Dust, Ice Fog and Thick Cloud Episodes**
2 **observed and modelled above Dome C, Antarctica**

3

4 **Philippe Ricaud¹, Eric Bazile¹, Massimo del Guasta², Christian Lanconelli^{3,4}, Paolo**
5 **Grigioni⁵, Achraf Mahjoub¹**

6

7 ¹Météo-France/CNRM, CNRS UMR 3589, 42 avenue Gaspard Coriolis, 31057 Toulouse,
8 France

9 ²INO-CNR, Via Madonna del Piano 10, 50019, Sesto Fiorentino, Italy

10 ³Institute of Atmospheric Sciences and Climate (ISAC), Consiglio Nazionale delle Ricerche,
11 via Gobetti 101, 40129 Bologna, Italy;

12 ⁴Now at Joint Research Center, Institute for Environment and Sustainability (IES), Land
13 Resource Management Unit (H05), via Fermi, 21027 Ispra (VA), Italy

14 ⁵ENEA, Lungotevere Thaon di Revel, 76-00196 Roma, Italy

15

16 **Version V12, 27 March 2017**

17 **Revision – R2**

18 **Submitted to:** *Atmospheric Chemistry and Physics Discussions*

19

20 **Abstract**

21 Episodes of thick cloud and diamond dust/ice fog were observed during 15 March to 8 April
22 2011 and 4 to 5 March 2013 in the atmosphere above Dome C (Concordia station, Antarctica,
23 75°06'S, 123°21'E, 3233 m amsl). The objectives of the paper are mainly to investigate the
24 processes that cause these episodes based on observations and to verify whether operational
25 models can evaluate them. The measurements were obtained from the following instruments:
26 1) A ground-based microwave radiometer (HAMSTRAD, H₂O Antarctica Microwave
27 Stratospheric and Tropospheric Radiometers) installed at Dome C that provided vertical
28 profiles of tropospheric temperature and absolute humidity every 7 minutes. 2) Daily
29 radiosoundings launched at 12:00 UTC at Dome C. 3) A tropospheric aerosol Lidar that
30 provides aerosol depolarization ratio along the vertical at Dome C. 4) Down- and upward short-
31 and longwave radiations as provided by the Baseline Surface Radiation Network (BSRN)
32 facilities. 5) An ICE-CAMERA to detect at an hourly rate the size of the ice crystal grains
33 deposited at the surface of the camera. 6) Space-borne aerosol depolarization ratio from the
34 Cloud-Aerosol Lidar with Orthogonal Polarization (CALIOP) Lidar aboard the Cloud-Aerosol
35 Lidar and Infrared Pathfinder Satellite Observation (CALIPSO) platform along orbits close to
36 the Dome C station. The time evolution of the atmosphere has also been evaluated by
37 considering the outputs from the meso-scale AROME and the global-scale ARPEGE
38 meteorological models. Thick clouds are detected during the warm and wet periods (24-26
39 March 2011 and 4 March 2013) with high depolarization ratios (greater than 30%) from the
40 surface to 5-7 km above the ground associated with precipitation of ice particles and the
41 presence of a supercooled liquid water (depolarization less than 10%) clouds. Diamond dust
42 and/or ice fog are detected during the cold and dry periods (5 April 2011 and 5 March 2013)
43 with high depolarization ratios (greater than 30%) in the planetary boundary layer to a
44 maximum altitude of 100-300 m above the ground with little trace of precipitation. Considering

45 5-day back trajectories, we show that the thick-cloud episodes are attributed to air masses with
46 an oceanic origin whilst the diamond dust/ice fog episodes are attributed to air masses with
47 continental origins. Although operational models can reproduce thick cloud episodes in the free
48 troposphere, they cannot evaluate the diamond dust/ice fog episodes in the planetary boundary
49 layer because they require to use more sophisticated cloud and aerosol microphysics schemes.

50

51

52 **1. Introduction**

53 The impact of global warming has become obvious in high latitude regions, particularly in
54 the Arctic region, where melting ice and softening tundra are causing profound changes. The
55 environmental response of the Arctic is characteristically different from that of the Antarctic
56 because of differences in planetary geography and energy circulation. Over the past 50 years,
57 the west coast of the Antarctic Peninsula has been one of the most rapidly warming parts of the
58 planet. This warming is not only restricted to the land but can also be noted in the Southern
59 Ocean. For example, the warming of the Antarctic winter troposphere is more important than
60 anywhere on Earth with a rate of 0.5 to 0.7°C per decade measured over the last thirty years
61 (Turner et al., 2006). In Antarctica, the polar vortex is more intense, is colder and lasts longer
62 than in Arctic. The role of the Antarctic ice is important because it is one of the key parameters
63 in the regulation of air temperature near the surface. During the austral winter, in the absence
64 of solar radiation, the surface cools via infrared radiation emitted towards a very cold and very
65 dry atmosphere. In the austral summer, the absorption of solar radiation at shorter wavelength
66 produces a diurnal cycle and warms the surface while heating is limited by a high albedo
67 (Pirazzini, 2004; Hudson et al., 2006).

68 Changes in the abundance of water vapour (H₂O) influence directly (and indirectly via
69 clouds) the Earth's radiation budget and therefore affect climate change (Brasseur et al., 1999)
70 because H₂O is the main greenhouse gas that emits and absorbs in the infrared domain. With
71 an average altitude of 2500 m above sea level, the Antarctic Plateau is one of the coldest and
72 driest places of the planet, for instance with temperature less than -80 °C and integrated water
73 vapor amount less than 0.5 mm in winter at the Dome C station (e.g., Tomasi et al., 2012). For
74 these reasons, numerous studies focused on climate change (e.g., Hines et al., 2004), processes
75 in the atmospheric boundary layer (e.g., Argentini et al, 2005), reactive species interacting with
76 the snow (e.g., Davis et al., 2001) and astronomical site quality (e.g., Tremblin et al, 2011).

77 Clouds play an important role in the radiation budget of the Earth. Since they have large
78 spatial, seasonal and diurnal variability and they are poorly represented in climate models, large
79 differences are obtained by climate models when assessing the strength and the direction of the
80 cloud feedback on the Earth radiation balance (Dufresne and Bony, 2008). The interconnections
81 between the Antarctic, the middle latitudes and the tropics show that Antarctic clouds are an
82 important part of the global climate system (Lubin et al., 1998). Based on observations from
83 CloudSat and Cloud-Aerosol Lidar and Infrared Pathfinder Satellite Observation (CALIPSO)
84 satellites over the period 2006-2010 (Adhikari et al., 2012), it is found that the Antarctic Plateau
85 has the lowest cloud occurrence of the Antarctic continent (<30%). The continental region of
86 the Antarctic Plateau experiences cloud about 30% of the time at altitudes below 3 km and less
87 than 10% of the time above 5 km. Cloud occurrence over the western continental region is about
88 50% below 3 km and about 30% from the surface up to 8 km. Furthermore, whatever the season
89 considered, it is shown that multilayer clouds occur over Antarctica.

90 The Dome C station (Concordia) in Antarctica (75°06'S, 123°21'E, 3233 m above mean sea
91 level) is operated jointly by the French Polar Institute Paul-Emile Victor (IPEV) and the Italian
92 Institute Programma Nazionale Ricerche in Antartide (PNRA). The site is located on the
93 Antarctic plateau with 24 hours a day in summer and 24 hours of night in winter, a
94 climatological temperature between -40 °C and -20 °C in summer and -80 °C and -60 °C in
95 winter (Tomasi et al., 2006). Situated on top of a dome, there is no katabatic wind as in the case
96 of the costal station of Dumont d'Urville (66°S, 140°E, 0 m above sea level) since the average
97 wind rarely exceeds 5 m s⁻¹ throughout the year. When the temperature drops, water may
98 precipitate and light ice crystals may be suspended in the air with little trace of precipitation
99 producing a phenomenon referred to as diamond dust or ice fog depending on the size of the
100 crystals. At the Dome C station, numerous studies already focused on the diurnal and seasonal
101 variations of the atmospheric boundary layer (e.g., Ricaud et al., 2012).

102 The objectives of the paper are mainly to investigate the processes that cause the presence
103 of thick cloud and diamond dust/ice fog episodes above the Dome C station based on
104 observations and verify whether operational models can estimate them. By combining
105 measurements from several instruments installed at the station, together with space-borne
106 measurements and model outputs, we intend to study the nature of the clouds and the
107 meteorological processes that favored their formation by using parameters such as tropospheric
108 temperature and absolute humidity, integrated water vapour, nebulosity, long- and shortwave
109 up- and downward radiations, together with the vertical distribution of aerosol depolarization
110 ratios.

111 We concentrate our efforts on two episodes: 15 March to 8 April 2011 and 4 to 5 March
112 2013. Several instruments have been used: 1) A ground-based microwave radiometer
113 (HAMSTRAD, H₂O Antarctica Microwave Stratospheric and Tropospheric Radiometers)
114 installed at Dome C that provided vertical profiles of tropospheric temperature and absolute
115 humidity with a 7-min integration time. 2) Daily radiosoundings launched at 12:00 UTC at
116 Dome C. 3) A tropospheric aerosol Lidar that provides aerosol depolarization ratio along the
117 vertical at Dome C. 4) Down- and upward short- and longwave radiations as obtained from
118 secondary standard pyranometers and pyrgeometer installed at Dome C and belonging to the
119 Baseline Surface Radiation Network (BSRN). 5) An ICE-CAMERA to detect at an hourly rate
120 the size of the ice crystal grains deposited at the surface of the camera. 6) Space-borne aerosol
121 depolarization ratio from the Cloud-Aerosol Lidar with Orthogonal Polarization (CALIOP)
122 Lidar aboard the CALIPSO platform along orbits close to the Dome C station. The time
123 evolution of the atmosphere over the 1-month period in 2011 has also been evaluated by
124 considering the outputs from the meso-scale model AROME (Seity et al., 2011) in 3
125 configurations. 1) “Operational”, operating mode with a snow albedo of 0.80. 2) “Operational
126 with ice tuning”, as in “Operational” but with a setting of snow albedo that can reach up to 0.85.

127 And finally 3) “ARPEGE micro-physics”, as in “Operational with ice tuning” but includes the
128 physics of ARPEGE and a state-of-the-art scheme to represent the snow pattern taking into
129 account the roughness length. And finally, we will use the global-scale ARPEGE
130 meteorological analyses in 2013 selected over the Dome C station.

131 The manuscript is structured as follow. Section 2 presents all the data sets used in our study.
132 Section 3 investigates episode 1, namely the thick cloud and the diamond dust/ice fog episodes
133 during the 1-month period in 2011 considering the temporal evolution of the different
134 parameters above and in the surroundings of the Dome C station. Section 4 deals with episode
135 2 in 2013. The genesis of the thick cloud and the diamond dust/ice fog episodes is discussed in
136 Section 5. Finally, Section 6 concludes the study.

137

138 **2. Datasets**

139 **2.1. The HAMSTRAD Radiometer**

140 The HAMSTRAD (H₂O Antarctica Microwave Stratospheric and Tropospheric
141 Radiometers) instrument is a state-of-the-art microwave radiometer to probe the troposphere in
142 very cold and very dry environments in order to retrieve temperature and absolute humidity
143 vertical profiles, and IWV. Temperature profiles are obtained from the 51–59 GHz spectral
144 range, centered on the oxygen line. Absolute humidity profiles are retrieved from the 169–197
145 GHz spectral range, centred on the water vapour line. IWV is calculated from the water vapour
146 profile integrated along the vertical. Integration time is 7 min. The radiometer is presented in
147 Ricaud et al. (2010).

148 The instrument was sent to Dome C in January 2009. It has been running automatically
149 since January 2010. Science and validation studies using HAMSTRAD data are detailed in
150 Ricaud et al., 2012; 2013; 2014a-c; and 2015. All the HAMSTRAD data measured since 2009
151 are freely available at the following address:

152 <http://www.cnrm.meteo.fr/spip.php?article961&lang=en>. The radiometer sensitivity is very
153 high in the planetary boundary layer, high in the free troposphere and very weak in the upper
154 troposphere-lower stratosphere (Ricaud et al., 2015). The H₂O and temperature vertical
155 resolutions are ~20-50 m, ~100 m and ~500 m in the planetary boundary layer, in the free
156 troposphere and in the upper troposphere-lower stratosphere, respectively. Statistically, it has
157 been shown that, against radiosondes from 2009 to 2014, there is a 1-5 K cold bias below 4 km,
158 and a 5-10 K warm bias above, with a high time correlation (linear Pearson correlation
159 coefficient $r > 0.80$). There is a wet bias of 0.1-0.3 g m⁻³ below about 2 km and a dry bias of
160 ~0.1 g m⁻³ above, with a high time correlation below 4 km ($r > 0.70$). Yearly-averaged vertical
161 profiles of the biases in temperature and absolute humidity are also provided from 2009 to date
162 at the same http address. Note we have not debiased HAMSTRAD data in the present study.

163

164 **2.2. Radiosondes**

165 The programme of radiosoundings developed at Dome C is presented in Ricaud et al.
166 (2014a). Temperature and humidity biases against HAMSTRAD are shown in the previous
167 section. In the present study, the vertical profiles of temperature and humidity were taken from
168 RS92 radiosondes using the standard Vaisala evaluation routines without any correction of
169 sensor heating or time lag effect. We recall that the corrections performed on the radiosonde
170 data measured in 2009 according to Miloshevich et al. (2006) shown a weak impact (with a
171 maximum of +4% on IWV) on the vertical profiles (Ricaud et al., 2013). Furthermore,
172 considering the updated tools developed in Miloshevich et al. (2009), Tomasi et al. (2011 and
173 2012) found that, between 630 and 470 hPa, the correction factor for humidity estimated by the
174 radiosonde varied within 1.10-1.15 for daytime and within 0.98-1.00 for nighttime. It is
175 important to note that the 630-470 hPa layer is located between the ground and an altitude of

176 ~2 km which maximizes the calculation of IWV. A 1.2 K cold bias is also observed in the RS92
177 from the surface up to an altitude of ~4 km (Tomasi et al., 2011 and 2012).

178

179 **2.3. The Aerosol Lidar**

180 The aerosol lidar is an automatic backscatter and depolarization system in operation at
181 Dome C in relation with different scientific projects ([http://lidarmax.altervista.org/lidar/](http://lidarmax.altervista.org/lidar/Antarctic_LIDAR.php)
182 [Antarctic LIDAR.php](http://lidarmax.altervista.org/lidar/Antarctic_LIDAR.php)). Vertical profiles of aerosol and cloud structures are continuously
183 measured together with characterization of the physical phase of particles. Lidar data and false
184 color plots, obtained with an automated procedure, are delivered to Italy on a daily basis.

185 The Lidar system uses a Laser Quantel (Brio) at Dome C and operates at 532 nm to get
186 backscattering and depolarization ratio from 30 to 7000 m above ground with a 7.5-m vertical
187 resolution. The line of sight is zenith looking through a window enabling measurements in all-
188 weather conditions. The telescope has a 10-cm diameter, with 30-cm refractive optics and 0.15-
189 nm interference filter. It has already been used in several scientific studies, e.g. the radiative
190 properties of H₂O and clouds in the far infrared over Antarctica (Palchetti et al., 2015).

191

192 **2.4. CALIOP onboard CALIPSO**

193 The CALIPSO satellite has been launched to study the role clouds and aerosols play in the
194 Earth system that includes air quality, weather and climate. CALIPSO was launched on 28 April
195 2006 with the cloud profiling radar system on the CloudSat satellite. The CALIPSO satellite
196 comprises three instruments, the CALIOP Lidar, the Imaging Infrared Radiometer (IIR), and
197 the Wide Field Camera (WFC) (Winker et al., 2009).

198 CALIOP is a two-wavelength (532 nm and 1064 nm) polarization-sensitive lidar that
199 provides high-resolution vertical profiles of aerosols and clouds
200 (<https://calipso.cnes.fr/en/CALIPSO/lidar.htm>). CALIOP uses three receiver channels: one

201 measures the 1064 nm backscatter intensity and two channels measure orthogonally polarized
202 components of the 532 nm backscattered signal. The receiver telescope is 1 metre in diameter.
203 The full-angle field of view of the telescope is 130 μ rad resulting in a footprint at the Earth's
204 surface of about 90 metres. Algorithms have been developed to retrieve aerosols and cloud
205 layers together with optical and microphysical properties (Young and Vaughan, 2009).
206 Depolarization ratio estimated with version V3.01 is presented in our study.

207

208 **2.5. The BSRN Network**

209 The objective of the World Climate Research Programme (WCRP) Baseline Surface
210 Radiation Network (BSRN) is to provide, using a high sampling rate, observations of the best
211 possible quality, for short- and longwave surface radiation fluxes. These readings are taken
212 from a small number of selected stations, including Dome C, in contrasting climatic zones,
213 together with collocated surface and upper air meteorological data and other supporting
214 observations. The incoming longwave and shortwave radiation components of the surface
215 radiative balance were taken from the Dome C BSRN station, and measured with two Kipp &
216 Zonen CM22 secondary standard pyranometers and two Kipp & Zonen CG4 Pyrgeometers, all
217 operated according to BSRN guidelines (Lanconelli et al., 2011).

218

219 **2.6. The ICE-CAMERA**

220 At Dome C in 2013, an ICE-CAMERA was installed on the roof of the shelter where both
221 the HAMSTRAD and the aerosol Lidar were set up. This camera was able to take on an hourly
222 rate a picture of the ice crystal grains deposited at the surface of the camera. The ICE-CAMERA
223 (http://lidarmax.altervista.org/englidar/_Antarctic%20Precipitation.php) is equivalent to a
224 flatbed scanner. It was built in order to operate unattended in Polar Regions for the study of
225 precipitating ice grains. Precipitation is collected on a glass plate, where it is photographed with

226 5 μm resolution hourly. After each scan, the glass plate is electrically-heated in order to
227 sublimate the ice grains. Image-processing software is used for the automatic characterization
228 and counting of grains.

229

230 **2.7. The AROME Model**

231 AROME is a small-scale numerical prediction model, operational at Meteo-France since
232 December 2008. It was designed to improve short-range forecasts of severe events such as
233 intense Mediterranean precipitations (Cévenole events), severe storms, fog, urban heat during
234 heat waves. The physical parameterizations of the model come mostly from the MESO-NH
235 model whereas the dynamic core is the ALADIN model. The size of the mesh is 2.5 km against
236 10 km for ARPEGE over France in 2014. The model is initialized from a 3D-var data
237 assimilation system using radar reflectivity and Doppler wind. Five daily forecasts are made
238 with AROME, thus helping to better predict meteorological events of the day and of the morrow
239 (30 h forecast range). AROME was used within the GEWEX Atmospheric Boundary Layer
240 Study 4 (GABLS4) to study the meteorological evolution over the Dome C station (Bazile et
241 al., 2015).

242 For the study, three experiments at 2.5 km were used. Two based on the AROME con-
243 figurations: 1) "Operational", operating mode with the default snow scheme (Douville et al.,
244 1995) (labeled as 79HA). 2) "Operational with ice tuning", as in "Operational" but with a
245 setting of a minimum snow albedo of 0.8 (labeled as 79YG). In the third one "ARPEGE micro-
246 physics", the AROME physics was replaced by the ARPEGE one used in the global model with
247 the state-of-the-art scheme to represent the permanent snow with a minimum snow albedo of
248 0.8 valid over Dome C and a more accurate roughness length (labeled as 79Z6).

249

250

251 **2.8. The ARPEGE Model**

252 The ARPEGE model is the global model used for the numerical weather prediction (NWP)
253 at Météo-France. In the present study, the operational configuration has been used with a
254 stretched grid at high resolution over France (10 km) and a coarser grid over Australia of 60
255 km. At the South Pole, the horizontal resolution is about 50 km and the vertical grid has 70
256 levels with a first level at around 16 m above the ground. The assimilation tool is based on an
257 incremental 4-dimensional variational (4D-Var) method. The physical package used in the
258 ARPEGE model is at the state-of-the-art, with a Turbulent Kinetic Energy scheme associated
259 with a mass flux scheme for the boundary layer (Bazile et al., 2011). The clouds and the micro-
260 physics use 4 prognostic variables such as cloud water, cloud ice, rain and snow (Lopez, 2002;
261 Bouteloup et al., 2005). The radiative transfer in the atmosphere is computed with the Rapid
262 Radiative Transfer Model (RRTM) scheme (Mlawer et al., 1997) for the longwave and the
263 shortwave with the Fouquart-Morcrette scheme (Fouquart and Bonnel, 1980; Morcrette et al.,
264 2001).

265

266 **3. Episode 1 on 15 March-8 April 2011**

267 **3.1. Clouds**

268 In order to check whether clouds are present or not over the station during the two periods
269 studied in detail, we consider the time evolution of the aerosol depolarization as measured by
270 the Lidar installed at Dome C on 24-26 March and on 4-6 April 2011 (Fig. 1). On 24-26 March
271 (Fig. 1 top), high depolarization ratios (greater than 30%), signature of ice particles, start
272 increasing by the end of 24 March (22:00 UTC), reaching an altitude of 1.2-1.5 km, all over 25
273 March, and start decreasing on 26 March by 12:00 UTC. The vertical structures in the
274 depolarization ratio fields are a signature of precipitation of ice particles (Mishchenko et al.,
275 2000). On 26 March, at about 2 km altitude from 07:00 to 13:00 UTC, a layer of low

276 depolarization ratio (less than 14%) appears, that is a signature of liquid water cloud. In general,
277 over this period, the cloud is so opaque that the Lidar signal cannot penetrate the structure
278 beyond ~1.2 km altitude.

279 We gain more insight into the vertical structure of the cloud covering the Dome C station
280 by considering the space-borne CALIOP Lidar nighttime measurements performed on 25
281 March 2011 in the vicinity of the station. Figure 2 top left shows the Spaceborne Lidar CALIOP
282 measurements of depolarization ratio along one orbit in the vicinity of the Dome C station on
283 25 March 2011. We note that, at the location of the Dome C station ($75^{\circ}06'S$, $123^{\circ}21'E$), the
284 depolarization ratio is greater than 0.4 (ice particles) from the ground (3233 m above mean sea
285 level, amsl) to about 10 km amsl, namely ~7 km above the ground. If we now combine the
286 downward and upward Lidar information, we can state that on 24-26 March 2011, a 7-km thick
287 ice cloud passed over the Dome C station and precipitated ice particles whilst, by the end of the
288 period, a low-altitude (~2 km) liquid water cloud was also present.

289 From Figure 1 bottom, high depolarization ratios (greater than 30%) from the Lidar
290 operating at Dome C start increasing by the middle of 4 April (12:00 UTC), reaching a
291 maximum altitude of 100 m, increasing up to 200 m on 5 April at 09:00 UTC, to finish
292 decreasing on 6 April by 12:00 UTC. The high depolarization ratio shows that the cloud is
293 constituted of ice crystals and, since there are no other layers higher in the troposphere, there is
294 little trace of precipitation. Considering the CALIOP space-borne Lidar measurements of
295 depolarization ratio (Fig. 2 top right) performed on 5 April 2011 in the vicinity of the Dome C
296 station, they also suggest a much thinner cloud from the ground to about 4 km amsl, namely
297 less than 1 km above the ground, with values ranging 0.1-0.2 (ice particles). Since there is little
298 precipitation and no presence of standard thick clouds above the station, the thin cloud episode
299 is traditionally attributed to a diamond dust/ice fog episode, rather frequent at the Dome C
300 station.

301 From Girard and Blanchet (2001), ice fog is distinguished from diamond dust by the high
302 concentration of ice crystal of smaller diameters. Ice fog, ice crystals are generally closer to
303 spherical shape and their number concentration exceeds 1000 L^{-1} while their mean diameter is
304 below $30 \mu\text{m}$. From Walden et al. (2003), the atmospheric ice crystals over the Antarctic Plateau
305 in winter is mainly constituted of three major types: diamond dust, blowing snow and snow
306 grains. When sorted by number, Lawson et al. (2006) attribute 30% of the crystals recorded at
307 the South Pole Station to rosette shaped (mixed-habit rosettes, platelike polycrystals, and rosette
308 shapes with side planes), 45% to diamond dust (columns, thick plates, and plates), and 25% to
309 irregular. By mass, the percentages are 57% rosette shapes, 23% diamond dust, and 20%
310 irregular. In the literature of the ice crystals over Antarctica and particularly over the Antarctic
311 Plateau, there is little mention of ice fog except some studies performed in the coastal areas of
312 e.g. McMurdo in Lazzara (2010). Based on Gultepe et al. (2015) and Arctic studies, the
313 maximum size for ice fog crystals is about $200 \mu\text{m}$ with diamond dust ice crystal sizes greater
314 than $200 \mu\text{m}$. In the Eastern Antarctic Plateau over all the seasons except summer, a strong
315 surface-based temperature inversion persists in which small ice crystals referred to as diamond
316 dust/ice fog form in the boundary layer (Walden et al., 2003). Classification of ice-cloud
317 particles is important to retrieve the shape of individual crystals and to estimate the radiative
318 impact of the clouds (Bailey and Hallett, 2009; Lindqvist et al., 2012). It is beyond the scope
319 of the present analysis to classify ice crystals measured over the Dome C station.

320 The time evolution of the nebulosity vs. height as calculated by AROME according to the
321 3 configurations over the period 25 March-8 April 2011 is displayed Figure 3. In two
322 configurations (operational and operational with ice tuning), clouds (traced by values of
323 nebulosity greater than 0.25) are calculated mainly over two single periods: 1) on 22 March
324 from 1 to 5 km, and 2) on 25-29 March from the ground to 6 km. Considering the third
325 configuration (ARPEGE microphysics), the period when clouds (traced by values of nebulosity

326 greater than 0.25) are present is much longer than the two first configurations since it almost
327 covers the entire time interval under consideration. There are indeed the two periods previously
328 cited, namely on 22 March, and 25-29 March, but they extend both in time (22-24 March and
329 25-30 March, respectively) and altitude (surface to 7 km). Other periods show some moderate
330 values of nebulosity (0.10-0.25) on 15-17, 20 March, and 2, 3, 4, 6-7 April. These calculated
331 clouds can be close to the ground or high in the free troposphere (4-6 km). In the three
332 configurations, high nebulosity values (greater than 0.8) are calculated close to the surface (0-
333 200 m). The AROME model tends to produce a sort of cloud residual in the planetary boundary
334 layer in the three configurations analyzed.

335

336 **3.2. Radiation**

337 The time evolution of the downward and upward short- and longwave radiations as
338 measured by the BSRN international network is displayed in Figure 4, together with the net
339 irradiance (difference between the downward and the upward fluxes) from 15 March to 8 April
340 2011. The diurnal cycle of solar irradiance fluxes is clearly evidenced with the obvious
341 maximum at local noon ranging between 350 W m^{-2} (at the beginning of the period) and 150
342 W m^{-2} (at the end of the period). Albedo over the whole period is found to range between 0.8
343 and 0.95 with daily minimum at local noon (not shown). The upward longwave radiation
344 emitted by the surface is generally greater than the downward irradiance in clear sky conditions,
345 while they became similar under overcast when thick cloudiness prevents radiative cooling.
346 Consequently, alternating day and night periods in March and April, the net irradiance is
347 negative except around local noon when it can be either positive or close to zero. But for the
348 two periods considered so far, namely on 25-26 March and on 5 April, the radiation budget is
349 significantly different from the average situation.

350 On 25 March, the longwave radiations (both downward and upward) are greater than the
351 shortwave radiations (both downward and upward) even at local noon. The resulting effect is
352 that the net irradiance is positive or close to zero over the whole period. This obviously indicates
353 that a thick cloud is shielding the downward shortwave radiation (coming from the Sun) and
354 increases the downward longwave radiation (coming from the cloud). Furthermore, there is a
355 great probability a thick cloud is present over the Dome C station.

356 On 5 April, the situation is radically different. There was no abrupt increase of longwave
357 downward radiation as on 25 March, so we can rule out the presence of a thick cloud above the
358 station. Nevertheless, the situation is atypical since, at local noon, the downward shortwave
359 radiation is only slightly greater than the upward shortwave radiation, and the net irradiance
360 does not exhibit an obvious diurnal cycle maximizing at local noon. Consequently, even if the
361 presence of a thick cloud has been ruled out from the longwave radiation analysis, both the
362 shortwave and the total irradiance analyses tend to suggest the presence of a cloud, probably
363 thin and/or close to the surface, in order to 1) slightly affect the downward longwave irradiance,
364 and 2) strongly affect the diurnal cycle of the net irradiance. The next section investigates the
365 evolution of temperature and water vapour over the same period.

366

367 **3.3. Temperature and water vapour time evolutions**

368 The time evolution of temperature and absolute humidity profiles as measured by
369 HAMSTRAD from 0 to 5 km are shown Figures 5 and 6, respectively. In general, temperature
370 and water vapour from HAMSTRAD show a maximum over the period 25-26 March (thick
371 cloud episode) and a minimum over the period 5 April (diamond dust/ice fog episode). Along
372 the vertical, these two episodes cover a wide domain from the ground to more than 3 km above
373 the ground for temperature and up to 2.5-3 km above the ground for absolute humidity. The
374 warm and wet period lasts 3-4 days and is associated with the thick cloud episode although the

375 cold and dry period is of a short duration, namely 1 day, and is associated with the diamond
376 dust/ice fog episode. Note that the time evolution of temperature and water vapour over the 15
377 March-8 April 2011 as measured by HAMSTRAD is consistent with the one measured by the
378 radiosondes and calculated by AROME (not shown).

379

380 **4. Episode 2 on 4-5 March 2013**

381 The second episode, which is much shorter than the first one, relies on the same datasets
382 presented in Section 3. The only difference is that the model analyses are only from the
383 meteorological operational model ARPEGE that routinely delivers since December 2011 every
384 6 hours (00:00, 06:00, 12:00, and 18:00 UTC) meteorological fields at the vicinity of the Dome
385 C station.

386

387 **4.1. Clouds**

388 The depolarization ratio measured by the aerosol Lidar installed at Dome C from 4 to 5
389 March is shown on Figure 7. High depolarization ratios (greater than 30%) are present all over
390 4 March, reaching an altitude of 1.5-2.0 km, and start decreasing on 5 March by 00:00 UTC.
391 The thick cloud shows vertical structures in the depolarization ratio fields that are a signature
392 of precipitation of ice particles (see section 3.1). Between 13:00 and 14:00 UTC on 4 March
393 and from 00:00 to 10:00 UTC on 5 March, depolarization ratios are much lower, reaching
394 values of less than 10%. From 10:00 to 24:00 UTC on 5 March, depolarization ratios (Fig. 7)
395 are very high (>40%), indicative of ice crystals, but confined from the surface to 100-200 m
396 altitude indicative of the presence of diamond dust/ice fog. This is confirmed by the BSRN
397 radiation measurements (see section 4.2).

398 We now can consider the time evolution of the number of ice crystals measured by the ICE-
399 CAMERA integrated over one hour from 4 to 5 March 2013 above the Dome C station on

400 Figure 8. We notice that, from 00:00 to 10:00 UTC on 5 March, the number of ice crystals
401 detected by the ICE-CAMERA dramatically decreased from ~700 to ~200, whatever the crystal
402 ice habit size greater than 20 μm . There is also a strong Lidar raw signal (not shown) together
403 with a low Lidar depolarization signal (Fig. 7) around 100 m, signature of liquid particles.
404 Consequently, the reduced polarization detected in Fig. 7 reflects the presence of supercooled
405 liquid water and not the presence of ice crystals. There are some traces of vertical structures
406 present around 18:00 UTC, signature of precipitation, but very difficult to detect probably
407 because the fall velocity of the ice crystals is much less than in the case of thick clouds. But it
408 is beyond the scope of the present paper to discuss the fall velocity of the ice crystals.

409 Over this 2-day period, only one CALIOP/CALIPSO orbit has been analyzed in the vicinity
410 of the Dome C station (Fig. 1 bottom) on 4 March (08:15 UTC) during the thick-cloud episode.
411 On that day, the depolarization ratio is ranging 0.1-0.3 from the ground (3233 m amsl) to about
412 8 km amsl, namely ~5 km above the ground. Note that there is no CALIPSO orbit in the vicinity
413 of the Dome C station in coincidence with the diamond dust/ice fog episode.

414 Now we consider the presence of clouds and/or ice/liquid particles over the 2-day period
415 either from active and passive remote-sensing measurements or from ARPEGE analyses. The
416 time evolution of ice water mixing ratio calculated by ARPEGE over Dome C is represented in
417 the Figure 9 top together with the total precipitation flux over the 2-day period (Fig. 9 bottom).
418 The ARPEGE simulation indicates an ice cloud from the surface to near 4 km above the ground
419 on 4 March with the top altitude decreasing down to the surface on 5 March at 12:00 UTC. The
420 main thick cloud calculated on 4 March is associated with ice precipitation from the altitude of
421 ~3 km at 06:00 UTC down to ~2 km on 20:00 UTC (Fig. 9 bottom). This is in agreement with
422 observations. Between 18:00 and 24:00 UTC on 5 March, there is also a trace of ice cloud from
423 0 to 1 km altitude. There is no longer trace of local precipitation after 03:00 UTC on 5 March.
424 But this calculated ice cloud is much deeper than the one observed by the Lidar.

425

426 **4.2. Radiation**

427 The time evolution of the downward and upward short- and longwave radiations as
428 measured by the BSRN international network is displayed in Figure 10, together with the net
429 irradiance (difference between the downward and the upward fluxes) from 1 to 9 March 2013.
430 As already presented in section 3.2, the diurnal cycle of solar irradiance fluxes mainly shows a
431 clear-sky period over the Dome C station, except over the period from 4 March at 00:00 UTC
432 to 6 March at 00:00 UTC. Indeed, on 4 March all day long, there is a net increase in the long-
433 wave downward radiation from 80 to 120 W m⁻² compared to the values from 1 to 3 March and
434 from 7 to 9 March when we can expect the station is under clear sky conditions. Furthermore,
435 from 12:00 to 24:00 UTC, the net irradiance is about -20 W m⁻² on 4 March, whilst it is usually
436 about -30 W m⁻² in clear sky conditions. Consequently, there is a great probability a thick cloud
437 is present over the Dome C station on 4 March during 24 h. On 5 March, between 12:00 and
438 24:00 UTC, the net irradiance is very low (about -50 W m⁻²) compared to values of about -30
439 W m⁻² in clear sky conditions. There is a slight increase of the longwave downward (90 W m⁻²)
440 and upward (140 W m⁻²) fluxes on 5 March compared to the fluxes in clear sky conditions
441 (70 and 120 W m⁻², respectively), but much less than fluxes in cloudy conditions (150 and 160
442 W m⁻², respectively). Consequently, this 12-hour period on 5 March can neither be attributed
443 to clear sky nor to thick cloud episodes. Quantitatively, over the period 1-8 March 2013 (Figure
444 10), considering clear sky days (excluding 4 and 5 March), the net irradiance between 14:00
445 and 17:00 UTC is -30.55 W m⁻² whilst on 4 March (thick cloud episode) the net irradiance has
446 increased to -16.75 W m⁻² and on 5 March (diamond dust/ice fog episode) the net irradiance
447 has decreased to -45.52 W m⁻².

448

449

450 **4.3. Temperature and water vapour evolutions**

451 The temperature and the water vapour anomalies over the 2-day period are represented in
452 the Figures 11 and 12, respectively as measured by HAMSTRAD and as calculated by
453 ARPEGE.

454 Considering the 0-K temperature anomaly isoline (Fig. 11), both datasets show a warm
455 period on 4 March (thick cloud episode) followed by a cold period on 5 March (diamond
456 dust/ice fog episode) from the surface to about 2.4 km above the ground on 4 March by
457 ARPEGE and to about 4.0 ± 0.5 km by HAMSTRAD. The 1.6-km difference between the
458 altitude of the 0-K temperature anomaly isoline in HAMSTRAD and in ARPEGE data sets on
459 4 March might be due to the poor vertical resolution of HAMSTRAD compared to ARPEGE.
460 Above this altitude, a cold period is followed by a warm period in the two datasets. Although
461 the HAMSTRAD data are noisier than the ARPEGE data, the maxima and minima are
462 consistently observed and calculated in the lowermost troposphere around 12:00-18:00 UTC
463 on 4 March and around 18:00-22:00 UTC on 5 March, respectively. From the surface to about
464 4-5 km altitude, both data sets also show a wet period (Fig. 12) on 4 March (thick cloud episode)
465 followed by a dry period (diamond dust/ice fog episode) on 5 March.

466 In general, in the lower troposphere, ARPEGE and HAMSTRAD temperature datasets are
467 very consistent to each other (see Fig. 11). If we now consider into detail the evolution of the
468 vertical temperature structures during the 2 episodes, using also radiosondes measurements at
469 12:00 UTC, interesting conclusions can be deduced from Figure 13. During the warm episode
470 (thick cloud) on 4 March, there is a sharp positive vertical temperature gradient at 12:00 and
471 18:00 UTC within the first 100-200 m altitude layer in the planetary boundary layer from a very
472 cold surface of about 230 K reaching a maximum of about 240-242 K. Above, the atmosphere
473 is rather isothermal and starts cooling around 400-800 m. All the datasets are very consistent to
474 each other. During the cold episode on 5 March, the lower troposphere is generally colder than

475 during the warm episode, but at 12:00 UTC there is no such a stable planetary boundary layer
476 as observed a day before since the vertical gradient is only of a 3 K over 500 m altitude instead
477 of 20 K over 200 m during the warm episode. Radiosonde, ARPEGE and HAMSTRAD profiles
478 are consistent to each other. At 18:00 UTC, in the core of the diamond dust/ice fog episode, the
479 vertical structure of the temperature observed by HAMSTRAD showing a positive gradient
480 (218 to 227 K from 100 to 500 m) is opposite to the negative gradient of ARPEGE temperature
481 (228 to 226 K from the surface to 400 m). Consistent with Figure 13, the radiative impact of
482 the thick cloud is to enlarge the net irradiance by about 15 W m^{-2} thus to locally increase
483 temperature as measured by HAMSTRAD and calculated by ARPEGE whilst the radiative
484 impact of the diamond dust/ice fog is to reduce the net irradiance by about 15 W m^{-2} thus to
485 locally decrease temperature as measured by HAMSTRAD but not calculated by ARPEGE.
486 Consequently, the ice cloud calculated by ARPEGE on 5 March over the vertical domain 0-1
487 km (Fig. 9) is certainly advected and cannot be considered as a diamond dust/ice fog episode
488 locally produced as suggested by the observations.

489 If we synthesize our findings, we can state the following. The time evolution of temperature,
490 absolute humidity, ice and aerosol fields obviously shows two episodes of abrupt changes.
491 Firstly, a warm and wet period is associated with a thick cloud that develops from the surface
492 to 5-8 km above the ground and is constituted of ice crystals that precipitate. Secondly, a cold
493 and dry period is associated with a thin cloud that develops close to the surface (100-200 m)
494 and is constituted of ice crystals with a longer suspension time in the air. This later episode is
495 known as diamond dust/ice fog episode. The operational models take into account interactions
496 between liquid and solid water phases but are unable to actually simulate the number of droplets
497 that depends on their sizes. Consequently, models can estimate the presence of thick clouds but
498 cannot reproduce diamond dust/ice fog episodes. A more sophisticated cloud microphysics such
499 as a two-moment scheme as LIMA (Liquid Ice Multiple Aerosols) scheme (Vié et al., 2016)

500 and an explicit aerosol scheme (Girard et al., 2001) would favour the local production of ice
501 crystals in the planetary boundary layer.

502

503 **5. Discussions**

504 In this section, we investigate the processes that contributed to the presence of a thick-cloud
505 and a diamond-dust/ice-fog episode above the Dome C station considering the origin of air
506 masses, the integrated water vapour fields over Antarctica and the temperature and water vapour
507 budgets calculated by ARPEGE.

508

509 **5.1. Origin of Air Masses**

510 Both the impact of the origin of air masses on the short-term variability of H₂O and
511 temperature and the high correlation coefficient (greater than 0.90) between water vapour and
512 temperature at Dome C over the entire year 2010 were presented in Ricaud et al. (2012 and
513 2014c) based on 5-day back-trajectory calculations. We propose, in the present study, to use
514 the same methodology to interpret the time evolution of the atmosphere during the two above-
515 mentioned episodes. We have thus considered a 5-day back trajectory study based upon the
516 European Centre for Medium-Range Weather Forecasts (ECMWF) analyses starting from the
517 Dome C location at five different pressure levels from the planetary boundary layer (650 and
518 600 hPa), to the free troposphere (500, 400 and 300 hPa).

519 For episode 1, Figure 14 (top left) shows the 5-day back-trajectories at the 5 selected pressure
520 levels during the warm and wet period (see the section 3) on 25 March 2011 at 12:00 UTC
521 corresponding to the time of maximum temperature and absolute humidity of an air parcel
522 issued from Dome C. In the lowermost layers (650 and 600 hPa), the air parcels are mainly
523 issued from the Antarctic continent. But higher up, at 500, 400 and 300 hPa, air masses are
524 coming from the oceanic middle latitudes, between Australia and New Zealand, imprint of

525 warm and wet air masses. When air masses in the free troposphere reach the Antarctic continent,
526 they are uplifted and temperature decreases by more than 50 K (not shown). Note the air parcel
527 at 400 hPa that is firstly originated from oceanic high latitudes in the vicinity of the Antarctic
528 continent but moves towards the middle oceanic latitudes with a net subsidence and an increase
529 of temperature of 30 K.

530 Regarding the diamond-dust/ice-fog period, Figure 14 (top right) shows the 5-day back-
531 trajectories at the 5 selected pressure levels on 5 April 2011 at 12:00 UTC corresponding to the
532 time of minimum temperature and absolute humidity of an air parcel issued from Dome C. We
533 can note that all the calculated air masses are originated from the Antarctic plateau whatever
534 the pressure level considered. Consequently, as already studied in Ricaud et al. (2012 and
535 2014c), we thus expect that both temperature and H₂O tends to decrease on 5 April at 12:00
536 UTC compared to the surrounding periods because air masses with continental origins produce
537 a cold and dry atmosphere above Dome C (as on 5 April 2011).

538 For episode 2, Figure 14 bottom left shows the 5-day back-trajectories at the 4 selected
539 pressure levels of 650, 600, 500 and 400 hPa during the warm and wet period (see section 4)
540 on 4 March 2013 at 08:00 UTC corresponding to the time of maximum temperature and
541 absolute humidity of an air parcel issued from Dome C. At 650 hPa, the air parcel has a
542 continental origin but migrates very close to the coast 2 days before reaching Dome C. Above,
543 at 600, 500 and 400 hPa, all the air masses are coming from the oceanic middle-high latitudes
544 ranging from 47°S to 63°S and from the surface to ~680 hPa, namely imprint of warm and wet
545 air masses. As for episode 1, when air parcels in the free troposphere reach the Antarctic
546 continent, they are uplifted and temperature decreases by 20-30 K (not shown). On 5 March at
547 18:00 UTC (Fig. 14 bottom right) during the cold and dry period of episode 2 corresponding to
548 the time of minimum temperature and absolute humidity, the meteorological situation is
549 radically different. Whatever the pressure level considered, the air parcels are all confined to

550 the Antarctic plateau in the vicinity of the Dome C station, explaining again, as for episode 1,
551 the cold and dry atmosphere observed during episode 2.

552

553 **5.2. Integrated Water Vapour over Antarctica**

554 The Integrated Water Vapour (IWV) fields calculated by the NCEP/NCAR operational
555 analyses (Kalnay et al., 1996) on 25 March 2011 and 5 April 2011 for episode 1 over the
556 Antarctic continent (Figure 15 top left and right, respectively) show that the Eastern Antarctic
557 plateau is much wetter on 25 March than on 5 April. The IWV calculated over the Dome C
558 station is $\sim 1.4 \text{ kg m}^{-2}$ on 25 March 2011 and $\sim 0.6 \text{ kg m}^{-2}$ on 5 April 2011 in excellent agreement
559 with the HAMSTRAD measurements (see section 3.3). This is induced by the oceanic-origin
560 flux bringing warm and wet air masses over the Dome C station on 25 March and by the
561 continent-origin flux bringing cold and dry air masses over the station on 5 April. The same
562 exercise can be performed for the episode 2 (Figure 15 bottom left and right, respectively)
563 considering the IWV fields as calculated by the NCEP/NCAR operational analyses on 4 and 5
564 March 2013. There, the IWV fields above Dome C show a similar pattern between 4 and 5
565 March but with a smaller wet inflection on 4 March compared to 5 March with daily averaged
566 values of ~ 0.6 and $\sim 0.4 \text{ kg m}^{-2}$, respectively consistent with the daily-averaged values obtained
567 at Dome C with HAMSTRAD (~ 0.55 and $\sim 0.30 \text{ kg m}^{-2}$, respectively). Consequently,
568 considering episodes 1 and 2, the thick-cloud episodes observed during the warm and wet
569 period above Dome C are attributed to air masses with an oceanic origin whilst the diamond
570 dust/ice fog episodes occurred during the cold and dry period are attributed to air masses with
571 continental origins.

572

573

574

575 **5.3. Temperature and Water Vapour Budgets**

576 Here, we attribute the tendencies of temperature calculated by ARPEGE during episode 2
577 among radiation, turbulence, microphysics, and total advection and the tendencies of water
578 vapour among turbulence, microphysics, and total advection. Figure 16 shows the temperature
579 budget calculated on 4 March 2013 over the warm and wet 12-h period 00:00-12:00 UTC and
580 on 5 March 2013 over the dry and cold 12-h period 06:00-18:00 UTC whilst Figure 17 focuses
581 on the water vapour budget.

582 For altitudes greater than ~ 100 m (3333 m amsl) above the ground on 4 March and greater
583 than ~ 200 m on 5 March, the temperature tendency of the warm (Fig. 16 left) and of the cold
584 (Fig. 16 right) periods is mainly dominated by the advection processes (red lines). This is fully
585 consistent with the interpretation of the origin of air masses (previous subsection).
586 Nevertheless, in the planetary boundary layer below approximately 100 m on 4 March and
587 below 200 m on 5 March, the temperature tendency of the two periods is also governed by the
588 vertical mixing done by the turbulent processes (green line). Indeed, turbulence always tends
589 to stabilize the atmosphere impacted by radiative or dynamical forcing. The effect of the
590 radiative cooling on the surface temperature and its impact on the boundary layer is clearly
591 shown on 5 March (Fig. 16 right).

592 As for temperature, the water vapour tendency of the two periods also needs to be separated
593 at ~ 100 and ~ 200 m above the ground on 4 and 5 March, respectively. Above these two limits,
594 the water vapour tendency of the warm period (Fig. 17 left) and of the cold (Fig. 17 right)
595 periods is governed by both the advection and the microphysical processes. On 4 March,
596 warmer and more humid air is advected (total water vapour tendency in Fig. 17 left and total
597 temperature advection in Fig. 16 left are positive), so the microphysics tend to create some
598 clouds by condensation (negative microphysics tendency, blue line on Fig. 17 left) with weak
599 precipitations close to the surface (~ 18 mm in 12 hours, not shown). On 5 March (Fig. 17 right),

600 the water vapour advection (red line) is negative so a drier air is advected toward the Dome C
601 station. Below ~200 m, advection, turbulence and microphysical (precipitation) processes
602 compete to dehydrate the planetary boundary layer.

603 In general, this reinforces our conclusions of thick cloud episodes driven by warm and wet
604 air masses of oceanic origin and of diamond dust/ice fog episodes driven by cold and dry air
605 masses of continental origin. Nevertheless, in the planetary boundary layer below
606 approximately ~100-200 m, the water vapour tendency of the two periods is competing between
607 advection, microphysical and turbulence processes.

608

609 **6. Conclusions**

610 The present study takes the opportunity of combining several measurements and operational
611 model outputs to study the short-term evolution of the Antarctic atmosphere above the Dome
612 C station focusing on episodes of thick cloud and diamond dust/ice fog. The objectives of the
613 paper are mainly to investigate the processes that cause these episodes based on observations
614 and to verify whether operational models can evaluate them. From 15 March to 8 April 2011
615 and from 4 to 5 March 2013, the atmosphere has been probed by several instruments. 1) A
616 ground-based microwave radiometer (HAMSTRAD) installed at Dome C that provided vertical
617 profiles of tropospheric temperature and absolute humidity with a 7-min integration time. 2)
618 Daily radiosoundings launched at 12:00 UTC at Dome C. 3) A tropospheric aerosol Lidar that
619 provides aerosol depolarization ratio along the vertical. 4) Down- and upward short- and
620 longwave radiations from an instrument installed at Dome C belonging to the BSRN network.
621 5) An ICE-CAMERA to detect at an hourly rate the size of the ice crystal grains deposited at
622 the surface of the camera. 6) Space-borne aerosol depolarization ratio from the CALIOP Lidar
623 aboard the CALIPSO platform along orbits close to the Dome C station.

624 The time evolution of the atmosphere over the 1-month period in 2011 has also been
625 evaluated by considering the outputs from the mesoscale model AROME in 3 configurations.
626 1) “Operational”, operating mode with a snow albedo of 0.80. 2) “Operational with ice tuning”,
627 as in “Operational” but with a setting of snow albedo that can reach up to 0.85. And finally 3)
628 “ARPEGE micro-physics”, as in “Operational with ice tuning” but includes the physics of
629 ARPEGE and a state-of-the-art scheme to represent the snow pattern taking into account the
630 roughness length. The ARPEGE global-scale meteorological model analyses gave the state of
631 the atmosphere and relevant prognostics (ice precipitation, temperature and water vapour
632 budget) on 4 and 5 March 2013.

633 Considering upward and downward active measurements of aerosols from two Lidars
634 installed at Dome C and aboard a spaceborne platform, respectively, together with downward
635 and upward longwave radiations, the signature of a thick cloud with high depolarization ratios
636 (greater than 30%) is detected during 2 periods (24-26 March 2011 and 4 March 2013) from
637 the surface to ~5-7 km above the ground with precipitation of ice particles and the presence of
638 a supercooled liquid water cloud with low depolarization ratios (~10%). These 2 periods are
639 shown to be warm and wet by considering HAMSTRAD and radiosonde measurements. Over
640 2 other periods (5 April 2011 and 5 March 2013), diamond dust and/or ice fog are detected with
641 high depolarization ratios (greater than 30%) in the planetary boundary layer to a maximum
642 altitude of 100-300 m above the ground with little trace of precipitation. These 2 periods are
643 shown to be cold and dry by considering HAMSTRAD and radiosonde measurements.

644 The presence of a thick cloud during the warm and wet periods of 2011 and 2013 is
645 calculated by the operational models of AROME and ARPEGE in the free troposphere
646 extending from the surface to ~6 km above the ground. In the three configurations of AROME,
647 high nebulosity values (greater than 0.8) are calculated close to the surface (0-200 m), almost
648 systematically in the two first configurations (operational and operational with ice tuning). The

649 AROME model tends to produce a sort of cloud residual in the planetary boundary layer in the
650 three configurations analyzed so the presence of a thin cloud close to the surface cannot be
651 ruled out. ARPEGE also calculates ice precipitation during the thick cloud event. But the
652 diamond dust/ice fog episodes have not been evaluated in the planetary boundary layer during
653 the cold and dry periods by the operational models. No liquid water clouds have been estimated
654 by the ARPEGE analyses. Although operational models can reproduce thick cloud episodes in
655 the free troposphere, they cannot evaluate the diamond dust/ice fog episodes in the planetary
656 boundary layer because they require to use more sophisticated cloud and aerosol microphysics
657 schemes.

658 Considering 5-day back trajectories from Dome C and global distributions of IWV over the
659 Antarctic in 2011 and 2013 tends to show that the thick-cloud episodes observed during the
660 warm and wet periods above Dome C can be attributed to air masses with an oceanic origin
661 whilst the diamond dust/ice fog episode occurring during the cold and dry periods can be
662 attributed to air masses with continental origins. Thus, diamond dust/ice fog episodes are driven
663 by local processes whilst thick cloud episodes are driven by regional processes. This is
664 confirmed by the ARPEGE temperature tendencies calculated during the warm and the cold
665 periods of 2013 that are mainly dominated by the advection components whilst the water vapour
666 tendencies are governed by both the advection and the microphysical processes.

667

668 **Acknowledgment**

669 The present research project HAMSTRAD programme (910) has been performed at the
670 Dome C station and was supported by the French Polar Intitute, Institut polaire français Paul-
671 Emile Victor (IPEV), the Institut National des Sciences de l'Univers (INSU)/Centre National
672 de la Recherche Scientifique (CNRS), Météo-France and the Centre National d'Etudes
673 Spatiales (CNES). The permanently manned Concordia station is jointly operated by IPEV and

674 the Italian Programma Nazionale Ricerche in Antartide (PNRA). We would like to thank all the
675 winterover personels who worked at Dome C on the different projects: HAMSTRAD, Routine
676 Meteorological Observations (RMO), aerosol Lidar and BSRN. Thanks to the British
677 Atmospheric Data Centre, which is part of the Natural Environment Research Council (NERC)
678 National Centre for Atmospheric Science (NCAS), for the calculation of trajectories and access
679 to European Centre for Medium-Range Weather Forecasts (ECMWF) data. We have used
680 NCEP Reanalysis data provided by the NOAA/OAR/ESRL PSD, Boulder, Colorado, USA,
681 from their Web site at <http://www.esrl.noaa.gov/psd/>. The authors also would like to thank the
682 CALIPSO science team for providing the CALIOP images at [http://www-](http://www-calipso.larc.nasa.gov/)
683 [calipso.larc.nasa.gov/](http://www-calipso.larc.nasa.gov/). HAMSTRAD data are available at
684 <http://www.cnrm.meteo.fr/spip.php?article961&lang=en>. RMO data are available at
685 <http://www.climantartide.it>. We finally would like to thank the **three** anonymous reviewers to
686 their fruitful comments.

687

688

689 **References**

- 690 Adhikari, L., Wang, Z. and Deng, M.: Seasonal variations of Antarctic clouds observed by
691 CloudSat and CALIPSO satellites, *J. Geophys. Res.*, 117, D04202,
692 doi:10.1029/2011JD016719, 2012.
- 693 Argentini, S., Viola, A., Sempreviva, A. M. and Petenko, I.: Summer boundary-layer height at
694 the plateau site of Dome C, Antarctica, *Bound.-Layer Meteor.*, 115, 409-422, 2005.
- 695 Bailey, M. P., and Hallett, J: A comprehensive habit diagram for atmospheric ice crystals:
696 Confirmation from the laboratory, AIRS II, and other field studies, *J. Atmos. Sci.*, 66, 2888-
697 2899, 2009.
- 698 Bazile, E., Marquet, P., Bouteloup, Y., and Bouysse, F.: The Turbulent Kinetic Energy (TKE)
699 scheme in the NWP models at Météo-France, ECMWF Proceedings “Workshop on Diurnal
700 cycles and the stable boundary layer”, 127-136, 2011.
- 701 Bazile, E., Couvreur, F., Le Moigne, P., and Genthon, C.: First Workshop on the GABLS-4
702 Intercomparison, GEWEX Newsletter, pp18-19, August 2015.
- 703 Bouteloup, Y., Bouysse, F., and Marquet, P.: Improvements of Lopez's prognostic large scale
704 cloud and precipitation scheme, *ALADIN Newsletter*, 28, 66-73, 2005.
- 705 Brasseur, G. P., Orlando, J. J., and Tyndall, G. S.: Atmospheric chemistry and global change,
706 2nd edition, Oxford University Press, New York, Oxford, ISBN-0-19-510521-4, 1999.
- 707 Davis, D., Nowak J. B., Chen G., Buhr M., Arimoto R., Hogan A., Eisele F., Mauldin L., Tanner
708 D., Shetter R., Lefer B., and McMurry P.: Unexpected high levels of NO observed at South
709 Pole, *Geophys. Res. Lett.*, 28, 3625-3628, 2001.
- 710 Douville, H., Royer, J.-F. and Mahfouf, J.-F.: A new snow parameterization for the Météo-
711 France climate model, Part I : Validation in stand-alone experiments, *Clim. Dynam.*, 12,
712 21-35, 1995.

713 Dufresne, J. L. and Bony, S.: An assessment of the primary sources of spread of global warming
714 estimates from coupled atmosphere-ocean models, *J. Climate*, 21, 5135-5144, 2008.

715 Fouquart, Y., and Bonnel, B.: Computations of solar heating of the earth's atmosphere: a new
716 parameterization, *Beitr. Phys. Atmosph.*, 53, 35-62, 1980.

717 Girard, E. and Blanchet, J. P.: Microphysical parameterization of Arctic diamond dust, ice fog,
718 and thin stratus for climate models. *J. Atmos. Sci.*, 58, 1181-1198, 2001.

719 Gultepe, I., Kuhn, T., Pavolonis, M., Calvert, C., Gurka, J., Heymsfield, A. J., Liu, P. S. K.,
720 Zhou, B., Ware, R., Ferrier, B., Milbrandt, J. and Berstein, B.: Ice fog in Arctic during
721 FRAM-ICE Fog project: Aviation and Nowcasting Applications, *Bull. Am. Meteor. Soc.*,
722 95, 211-226, 2014.

723 Hines, K. M., Bromwich, D. H., Rasch, P. J. and Iacono, M. J.: Antarctic clouds and radiation
724 within the NCAR climate models, *J. Climate*, 17, 1198–1212, doi:10.1175/1520-
725 0442(2004)017, 2004.

726 Hudson, S. R., Warren, S. G., Brandt, R. E., Grenfell, T. C., and Six, D.: Spectral bidirectional
727 reflectance of Antarctic snow: Measurements and parameterization, *J. Geophys. Res.*, 111,
728 D18106, doi:10.1029/2006JD007290, 2006.

729 Kalnay, E., Kanamitsu, M., Kistler, R., Collins, W., Deaven, D., Gandin, L., Iredell, M., Saha,
730 S., White, G., Woollen, J., Zhu, Y., Leetmaa, A., Reynolds, R., Chelliah, M., Ebisuzaki,
731 W., Higgins, W. Janowiak, J., Mo, K. C., Ropelewski, C., Wang, J., Jenne, R. and Dennis
732 Joseph, D.: The NCEP/NCAR 40-Year Reanalysis Project, *Bull. Amer. Meteor. Soc.*, 77,
733 437–471, 1996.

734 Lanconelli, C., Busetto, M., Dutton, E. G., König-Langlo, G., Maturilli, M., Sieger, R., Vitale,
735 V. and Yamanouchi, T.: Polar baseline surface radiation measurements during the
736 International Polar Year 2007-2009: *Earth System Science Data*, 3(1), 1-8,
737 doi:10.5194/essd-3-1-2011, 2011.

738 Lawson, R. P., Baker, B. A., Zmarzly, P., O'Connor, D., Mo, Q., Gayet, J. F. and Shcherbakov,
739 V.: Microphysical and optical properties of atmospheric ice crystals at South Pole Station,
740 J. Appl. Meteor., 45, 1505-1524, 2006.

741 Lazzara, M.: Diagnosing Antarctic fog, 5th International Conference on Fog, Fog Collection
742 and Dew, Münster, Germany, 25-30 July 2010. Vol. 1, p. 150.
743 (<http://meetingorganizer.copernicus.org/FOGDEW2010/FOGDEW2010-150.pdf>)

744 Lindqvist, H., Muinonen, K., Nousiainen, T., Um, J., McFarquhar, G. M., Haapanala, P.,
745 Makkonen, R. and Hakkarainen, H.: Ice-cloud particle habit classification using principal
746 components, J. Geophys. Res., 117, D16206, doi:10.1029/2012JD017573, 2012.

747 Lopez, P.: Implementation and validation of a new prognostic large-scale cloud and
748 precipitation scheme for climate and data assimilation purposes, Q. J. R. Meteorol. Soc.,
749 128, 229-257, 2002.

750 Lubin, D., Chen, B., Bromwich, D. H., Somerville, R. C., Lee, W. H., and Hines, K. M.: The
751 Impact of Antarctic Cloud Radiative Properties on a GCM Climate Simulation, J. Climate,
752 11, 447-462, 1998.

753 Miloshevich, L. M., Vömel, H., Whiteman, D. N., Lesht, B. M., Schmidlin, F. J. and Russo, F.:
754 Absolute accuracy of water vapor measurements from six operational radiosonde types
755 launched during AWEX-G and implications for AIRS validation, J. Geophys. Res., 111,
756 D09S10, doi:10.1029/2005JD006083, 2006.

757 Miloshevich, L. M., Vömel, H., Whiteman, D. N. and Leblanc, T.: Accuracy assessment and
758 corrections of Vaisala RS92 radiosonde water vapour measurements, J. Geophys. Res., 114,
759 D11305, doi:10.1029/2008JD011565, 2009.

760 Mishchenko, M. I., J. W. Hovenier, and L. D. Travis (Eds.): Light Scattering by Nonspherical
761 Particles: Theory, Measurements, and Applications. Academic Press. Chapter 14, 393-416,
762 2000.

763 Mlawer, E. J., Taubman, S. J., Brown, P. D., Iacono, M. J. and Clough, S. A.: Radiative transfer
764 for inhomogeneous atmospheres: RRTM, a validated correlated-k model for the longwave,
765 J. Geophys. Res., 102D, 16663-16682, 1997.

766 Morcrette, J.-J., Mlawer, E. J., Iacono, M. J. and Clough, S. A.: Impact of the radiation transfer
767 scheme RRTM in the ECMWF forecasting system, ECMWF Newsletter, 91, 2-9, 2001.

768 Palchetti, L., Bianchini, G., Di Natale, G., and Del Guasta, M.: Far infrared radiative properties
769 of water vapor and clouds in Antarctica, B. Am. Meteorol. Soc., 96, 1505-1518,
770 doi:10.1175/BAMS-D-13-00286.1, 2015

771 Pirazzini, R.: Surface albedo measurements over Antarctic sites in summer, J. Geophys. Res.,
772 109, D20118, doi:10.1029/2004JD004617, 2004.

773 Ricaud, P., Gabard, B., Derrien, S., Chaboureau, J.-P., Rose, T., Mombauer, A. and Czekala,
774 H.: HAMSTRAD-Tropo, A 183-GHz Radiometer Dedicated to Sound Tropospheric Water
775 Vapor Over Concordia Station, Antarctica, IEEE Trans Geosci Remote Sens., 48, 1365–
776 1380, doi: 10.1109/TGRS.2009.2029345, 2010.

777 Ricaud, P., Genthon, C., Durand, P., Attié, J.-L., Carminati, F., Canut, G., Vanacker, J.-F.,
778 Moggio, L., Courcoux, Y., Pellegrini, A. and Rose, T.: Summer to Winter Diurnal
779 Variabilities of Temperature and Water Vapor in the lowermost troposphere as observed by
780 the HAMSTRAD Radiometer over Dome C, Antarctica, Bound.-Layer Meteor., 143, 227–
781 259, doi:10.1007/s10546-011-9673-6, 2012.

782 Ricaud, P., Carminati, F., Attié, J.-L., Courcoux, Y., Rose, T., Genthon, C., Pellegrini, A.,
783 Tremblin, P. and August, T: Quality Assessment of the First Measurements of Tropospheric
784 Water Vapor and Temperature by the HAMSTRAD Radiometer over Concordia Station,
785 Antarctica, IEEE Trans Geosci Remote Sens., 51, 3217–3239, doi:
786 10.1109/TGRS.2012.2225627, 2013.

787 Ricaud, P., Carminati, F., Courcoux, Y., Pellegrini, A., Attié, J.-L., El Amraoui, L., Abida, R.,
788 Genthon, C., August, T. and Warner, J.: Statistical Analyses and Correlation between
789 Tropospheric Temperature and Humidity at Dome C, Antarctica, *Antarct. Sci.*, 26, 290 –
790 308. doi:10.1017/S0954102013000564, 2014a.

791 Ricaud, P.: Variabilités de la vapeur d'eau et de la température troposphérique au Dôme C
792 (station Concordia), Antarctique. Partie I : l'instrument Hamstrad, *La Météorologie*, 84,
793 15-28, doi:10.4267/2042/53184, 2014b.

794 Ricaud, P.: Variabilités de la vapeur d'eau et de la température troposphérique mesurées par le
795 radiomètre micro-onde HAMSTRAD au Dôme C, Antarctique. Partie II : Résultats
796 scientifiques, *La Météorologie*, 85, 35-46, doi:10.4267/2042/53749, 2014c.

797 Ricaud, P., Grigioni, P., Zbinden, R., Attié, J.-L., Genoni, L., Galeandro, A., Moggio, A.,
798 Montaguti, S., Petenko, I. and Legovini, P.: Review of tropospheric temperature, absolute
799 humidity and integrated water vapour from the HAMSTRAD radiometer installed at Dome
800 C, Antarctica, 2009–14, *Antarct. Sci.*, 27, 598-616, doi:10.1017/S0954102015000334,
801 2015.

802 Seity, Y., Brousseau, P., Malardel, S., Hello, G., Bénard, P., Bouttier, F., Lac, C. and Masson,
803 V.: The AROME-France Convective-Scale Operational Model, *Mon. Wea. Rev.*, 139, 976–
804 991, 2011.

805 Tomasi, C., B. Petkov, E. Benedetti, V. Vitale, A. Pellegrini, G. Dargaud, L. De Silvestri, P.
806 Grigioni, E. Fossat, W.L. Roth, and L. Valenziano: Characterization of the atmospheric
807 temperature and moisture conditions above Dome C (Antarctica) during austral summer
808 and fall months, *J. Geophys. Res.*, 113, D20305, doi:10.1029/2005JD006976, 2006.

809 Tomasi, C., Petkov, B., Benedetti, E., Valenziano, L. and Vitale, V.: Analysis of a 4 year
810 radiosonde dataset at Dome C for characterizing temperature and moisture conditions of the
811 Antarctic atmosphere, *J. Geophys. Res.*, 116, D15304, doi:10.1029/2011JD015803, 2011.

812 Tomasi, C., Petkov, B. H. and Benedetti, E.: Annual cycles of pressure, temperature, absolute
813 humidity and precipitable water from the radiosoundings performed at Dome C, Antarctica,
814 over the 2005-2009 period, *Antarct. Sci.*, 24, 637–658, doi:10.1017/S0954102012000405,
815 2012.

816 Tremblin, P., V. Minier, N. Schneider, G. Al. Durand, M. C. B. Ashley, J. S. Lawrence, D. M.
817 Luong-van, J. W. V. Storey, G. An. Durand, Y. Reinert, C. Veyssiere, C. Walter, P. Ade,
818 P. G. Calisse, Z. Challita, E. Fossat, L. Sabbatini, A. Pellegrini, P. Ricaud and J. Urban:
819 Site testing for submillimetre astronomy at Dome C in Antarctica, *Astronomy and*
820 *Astrophysics*, 535 A112, DOI: <http://dx.doi.org/10.1051/0004-6361/201117345>, 2011.

821 Turner, J., Lachlan-Cope, T. A., Colwell, S., Marshall, G. J. and Connolley, W. M.: Significant
822 Warming of the Antarctic Winter Troposphere, *Science*, 311, doi:10.1126/science.1121652,
823 2006.

824 Vié, B., Pinty, J. P., Berthet, S., & Leriche, M. : LIMA (v1. 0): A quasi two-moment
825 microphysical scheme driven by a multimodal population of cloud condensation and ice
826 freezing nuclei. *Geosci. Model Dev.*, 9, 567-586, 2016.

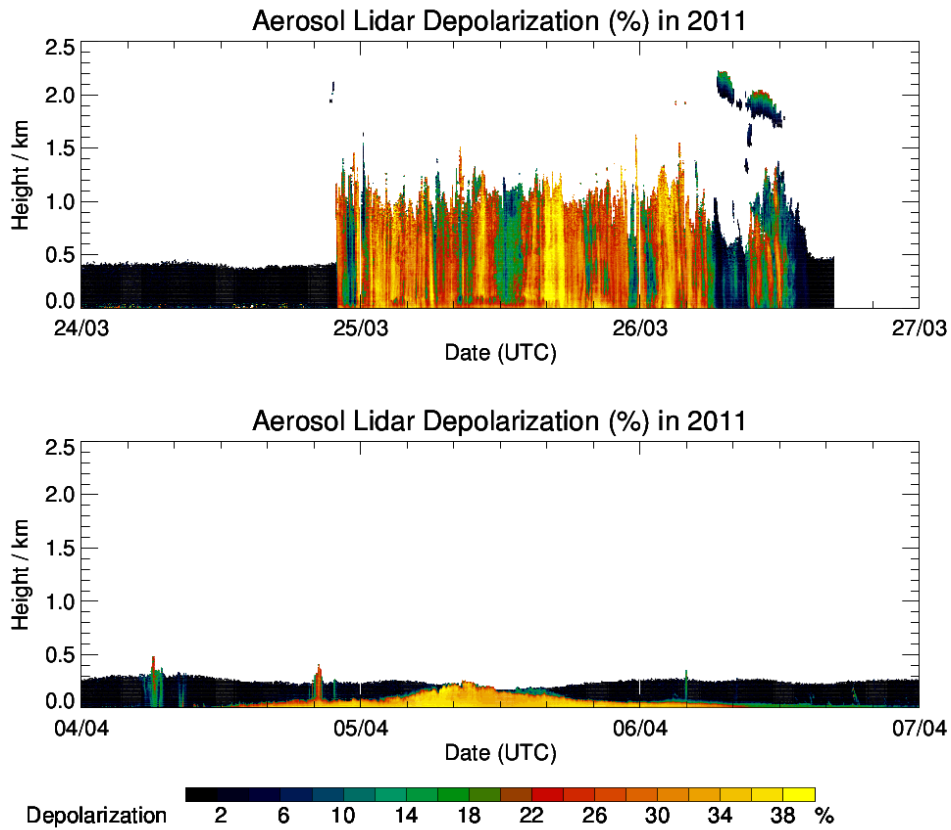
827 Walden, V. P., Warren, S. G. and Tuttle, E.: Atmospheric ice crystals over the Antarctic Plateau
828 in winter, *J. Appl. Meteorol.*, 42, 1391-1405, 2003.

829 Winker, D. M., Vaughan, M. A., Omar, A., Hu, Y., Powell, K. A., Liu, Z., Hunt, W. H. and
830 Young, S. A.: Overview of the CALIPSO mission and CALIOP data processing algorithms,
831 *J. Atmos. Oceanic Technol.*, 26, 2310-2323, 2009.

832 Young, S. A. and Vaughan, M. A.: The retrieval of profiles of particulate extinction from Cloud
833 Aerosol Lidar Infrared Pathfinder Satellite Observations (CALIPSO) lidar data: Algorithm
834 description, *J. Atmos. Oceanic Technol.*, 26, 1105–1119, 2009.

835

Figure Caption



837

838 **Fig. 1:** (Top, from left to right) Aerosol depolarization as measured by the Lidar installed at the

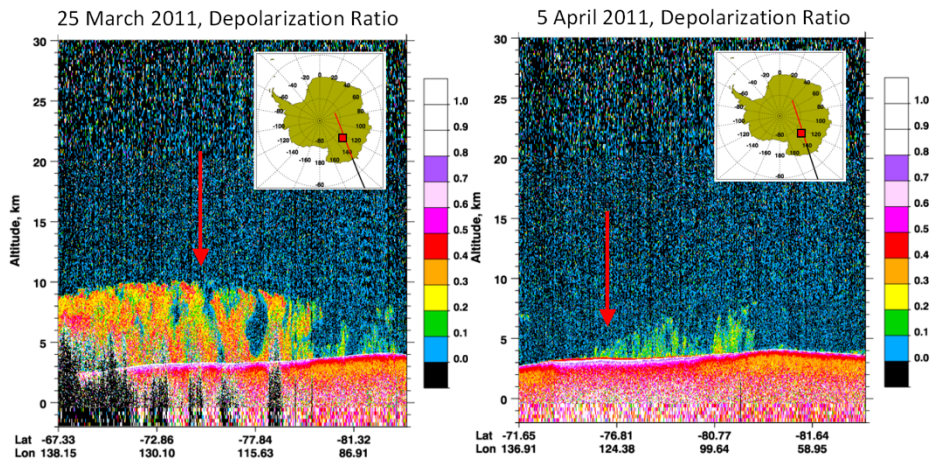
839 Dome C station over the period 24-26 March 2011. (Bottom, from left to right) Aerosol

840 depolarization as measured by the Lidar installed at the Dome C station over the period 4-6

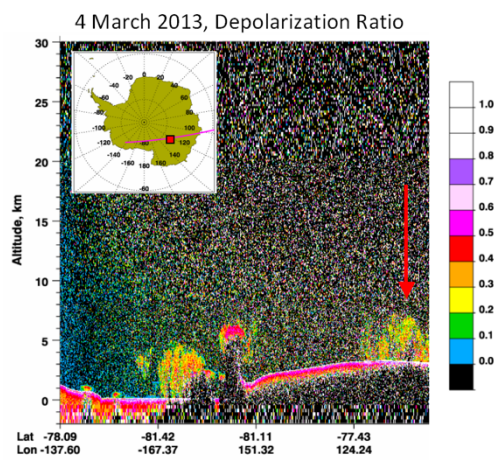
841 April 2011.

842

843



844

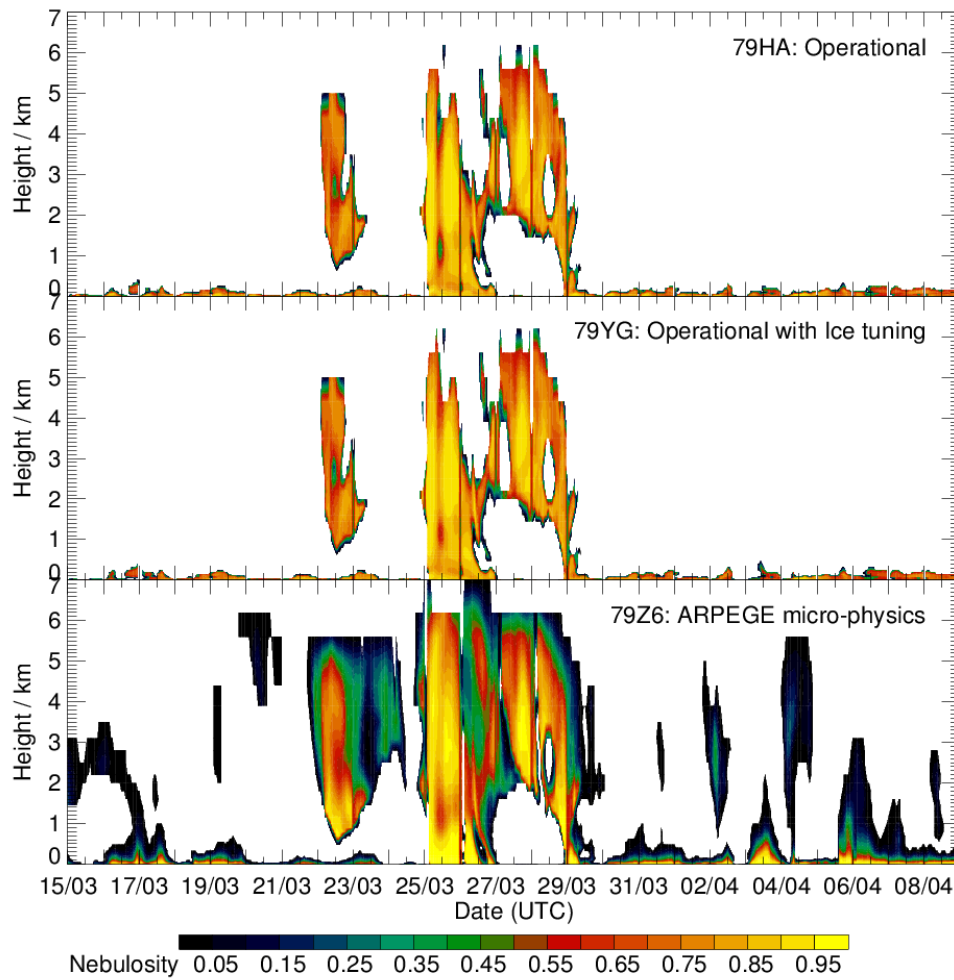


845 **Fig. 2:** Spaceborne Lidar CALIOP measurements of depolarization ratio along one orbit in the
846 vicinity of the Dome C station on 25 March 2011 (top left), 5 April 2011 (top right) and 4
847 March 2013 (bottom). The red square represents the location of the Dome C station. The red
848 vertical arrow represents the approximate location of the Dome C station.

849

850

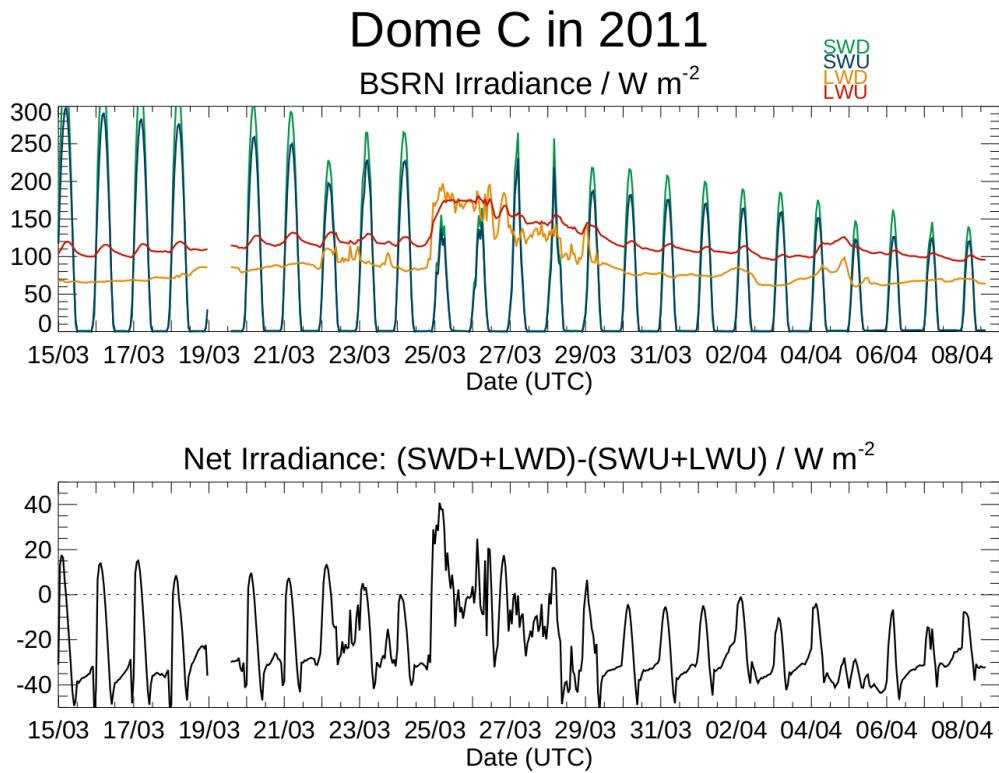
AROME at Dome C in 2011



851
852

853 **Fig. 3:** (From top to bottom) Time evolution of nebulosity from 15 March to 8 April 2011 above
854 Dome C as calculated by the mesoscale model AROME according to different runs: operational
855 (top), operational with ice tuning (center) and considering ARPEGE micro-physics (bottom).
856 See the text for further information regarding the AROME runs.

857

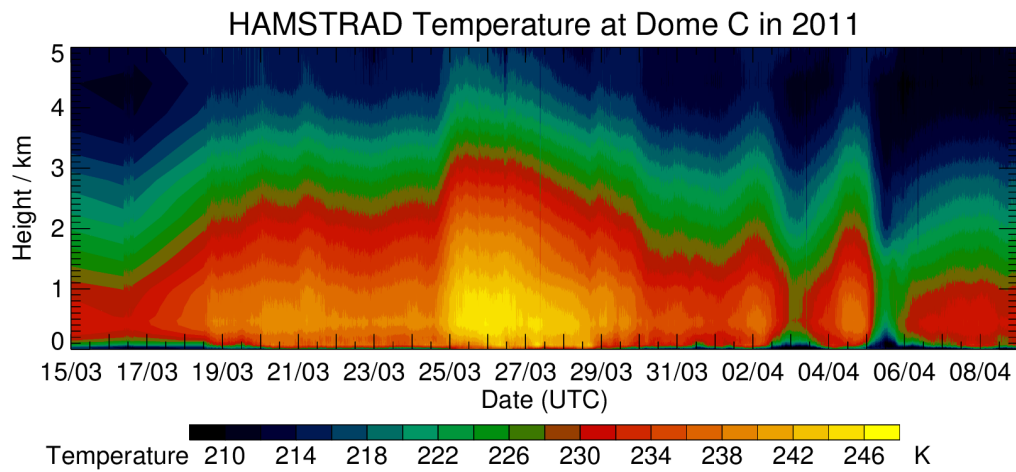


858

859 **Fig. 4:** (Top) Time evolution of downward shortwave radiation (SWD, green line), upward
 860 shortwave radiation (SWU, blue line), downward longwave radiation (LWD, orange line), and
 861 upward longwave radiation (LWU, red line) from 15 March to 8 April 2011 above Dome C as
 862 measured by the BSRN instruments. (Bottom) Net irradiance $(\text{SWD} + \text{LWD} - \text{SWU} - \text{LWU})$ as
 863 measured by the BSRN instruments.

864

865



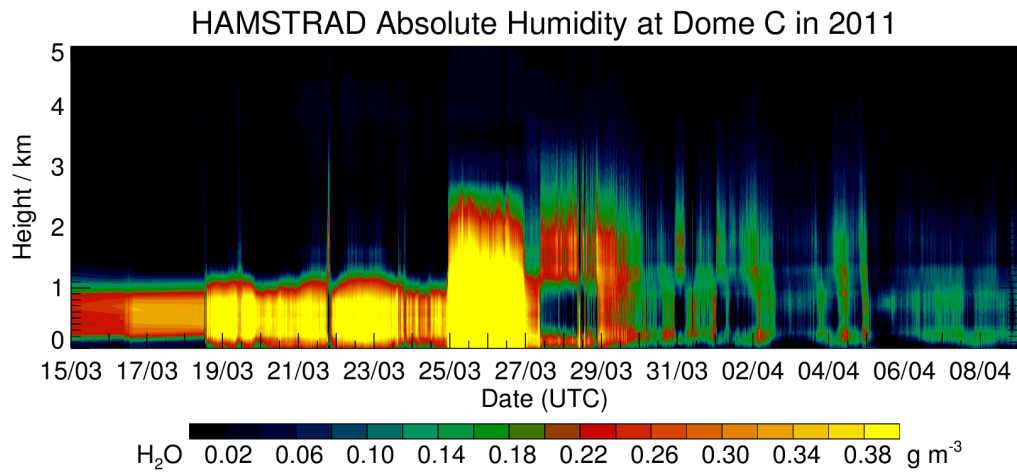
866

867 **Fig. 5:** Time evolution of temperature from 15 March to 8 April 2011 above Dome C as
 868 measured by the HAMSTRAD radiometer from 0 to 5 km.

869

870

871

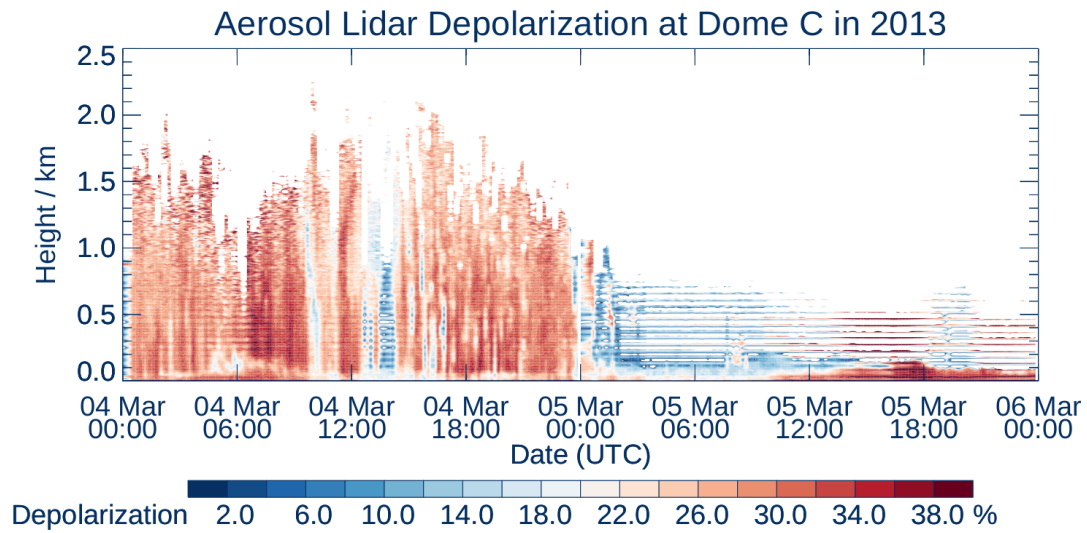


872

873 **Fig. 6:** Time evolution of absolute humidity from 15 March to 8 April 2011 above Dome C as
874 measured by the HAMSTRAD radiometer from 0 to 5 km.

875

876



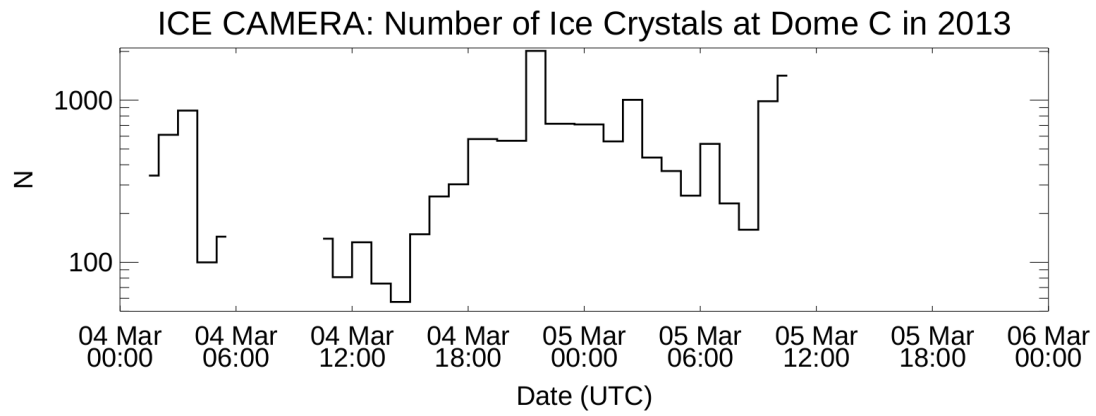
877

878 **Fig. 7:** Time evolution of the Depolarization ratio (%) from 4 to 5 March 2013 above the Dome

879 C station as measured by the aerosol Lidar installed at Dome C.

880

881



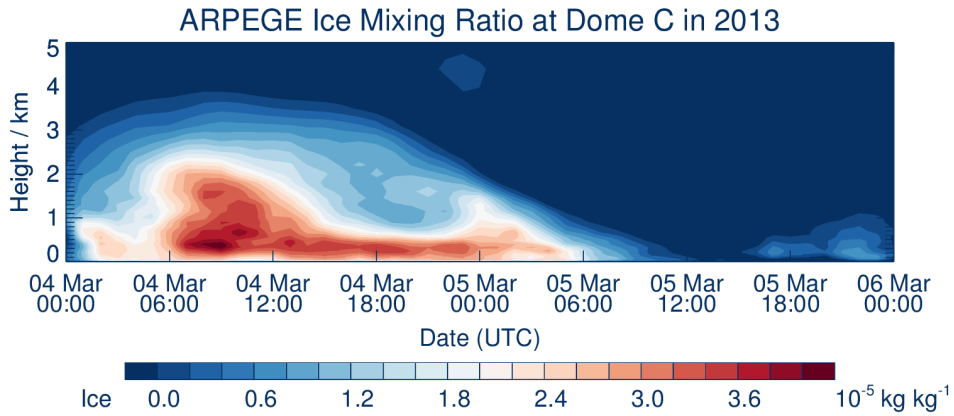
882

883 **Fig. 8:** Time evolution of the number of ice crystals measured by the ICE-CAMERA integrated

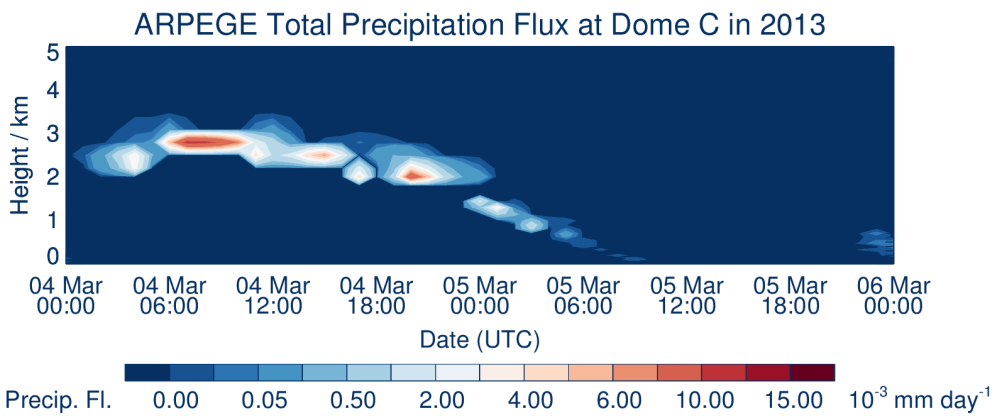
884 over one hour from 4 to 5 March 2013 above the Dome C station.

885

886



887

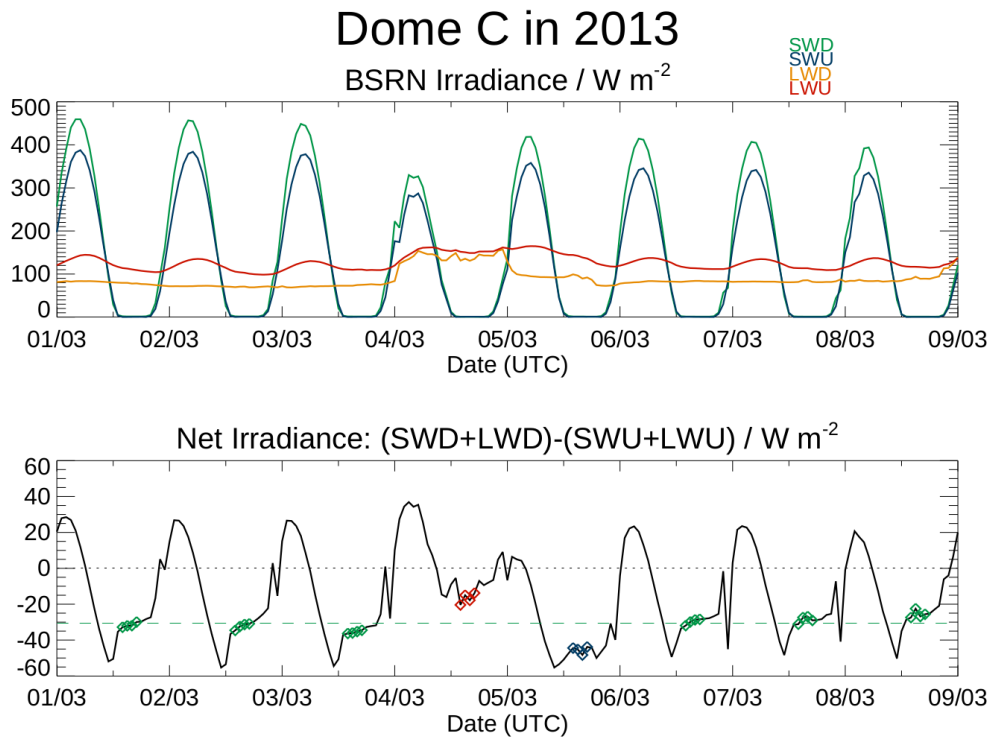


888

889 **Fig. 9:** Time evolution of the Ice Water Mixing ratio (top) and of the Total Precipitation Flux
 890 (bottom) from 4 to 5 March 2013 above the Dome C station as calculated by the ARPEGE
 891 model.

892

893



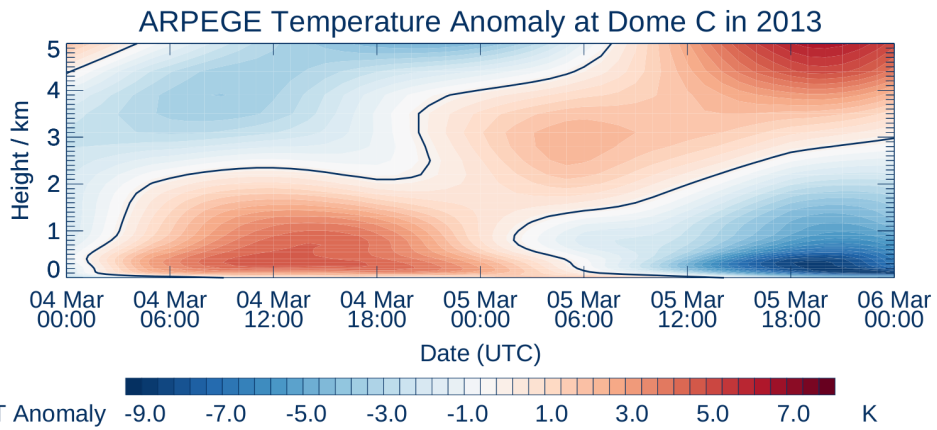
894

895 **Fig. 10:** (Top) Time evolution of downward shortwave radiation (SWD, green line), upward
 896 shortwave radiation (SWU, blue line), downward longwave radiation (LWD, orange line), and
 897 upward longwave radiation (LWU, red line) from 1 to 9 March 2013 above Dome C as
 898 measured by the BSRN instruments. (Bottom) Net irradiance (SWD+LWD-SWU-LWU) as
 899 measured by the BSRN instruments. The horizontal green dashed line represents the net
 900 irradiance averaged between 14:00 and 17:00 UTC (represented by green diamonds) from 1 to
 901 8 March excluding 4 and 5 March. The red and blue diamonds represent the net irradiances
 902 measured between 14:00 and 17:00 UTC on 4 March (thick cloud episode) and 5 March
 903 (diamond dust/ice fog episode), respectively.

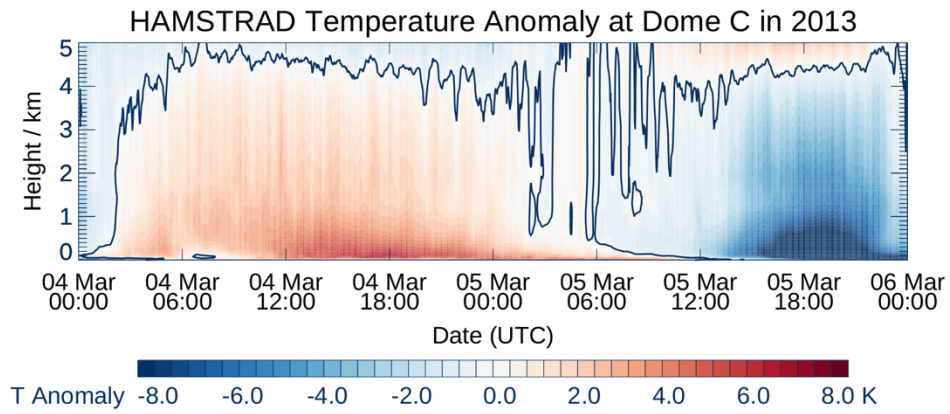
904

905

906



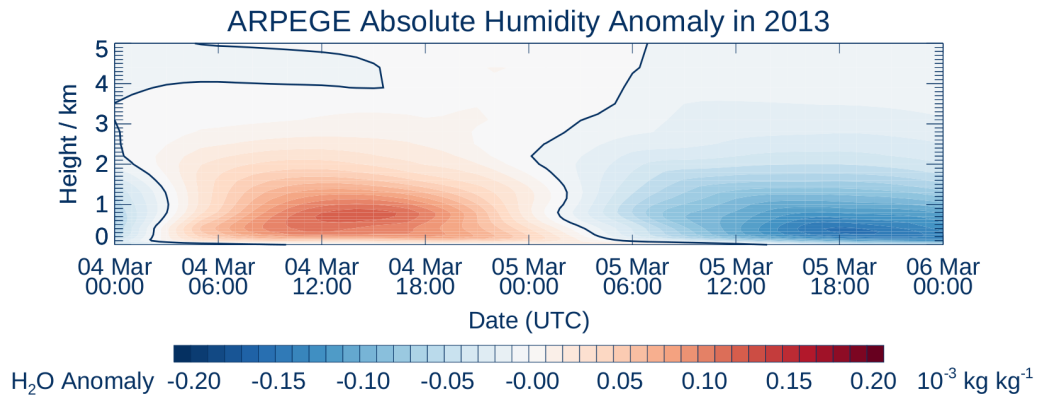
907



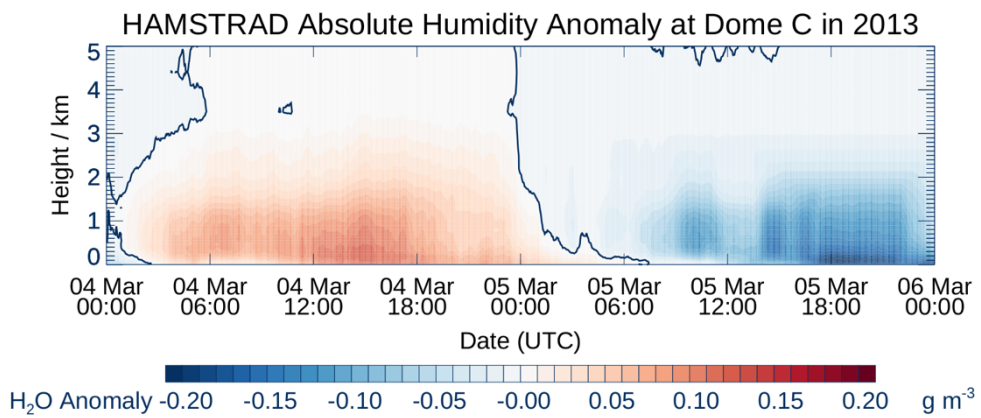
908

909 **Fig. 11:** Temperature anomaly from 4 to 5 March 2013 above the Dome C station as calculated
 910 by the ARPEGE model (top) and as measured by the HAMSTRAD radiometer (bottom).

911



912

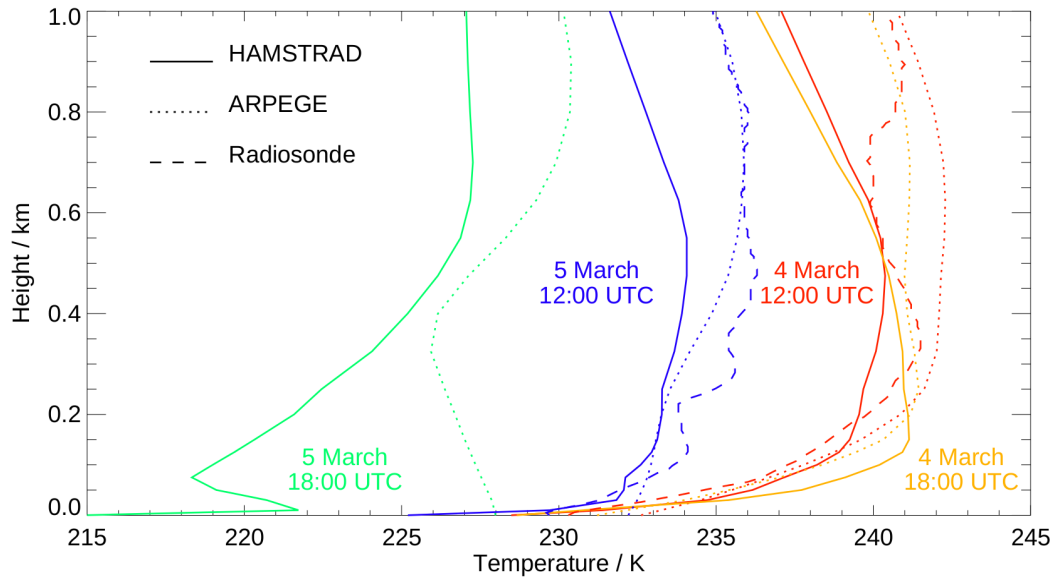


913

914 **Fig. 12:** Absolute Humidity anomaly from 4 to 5 March 2013 above the Dome C station as
 915 calculated by the ARPEGE model (top) and as measured by the HAMSTRAD radiometer
 916 (bottom).

917

918



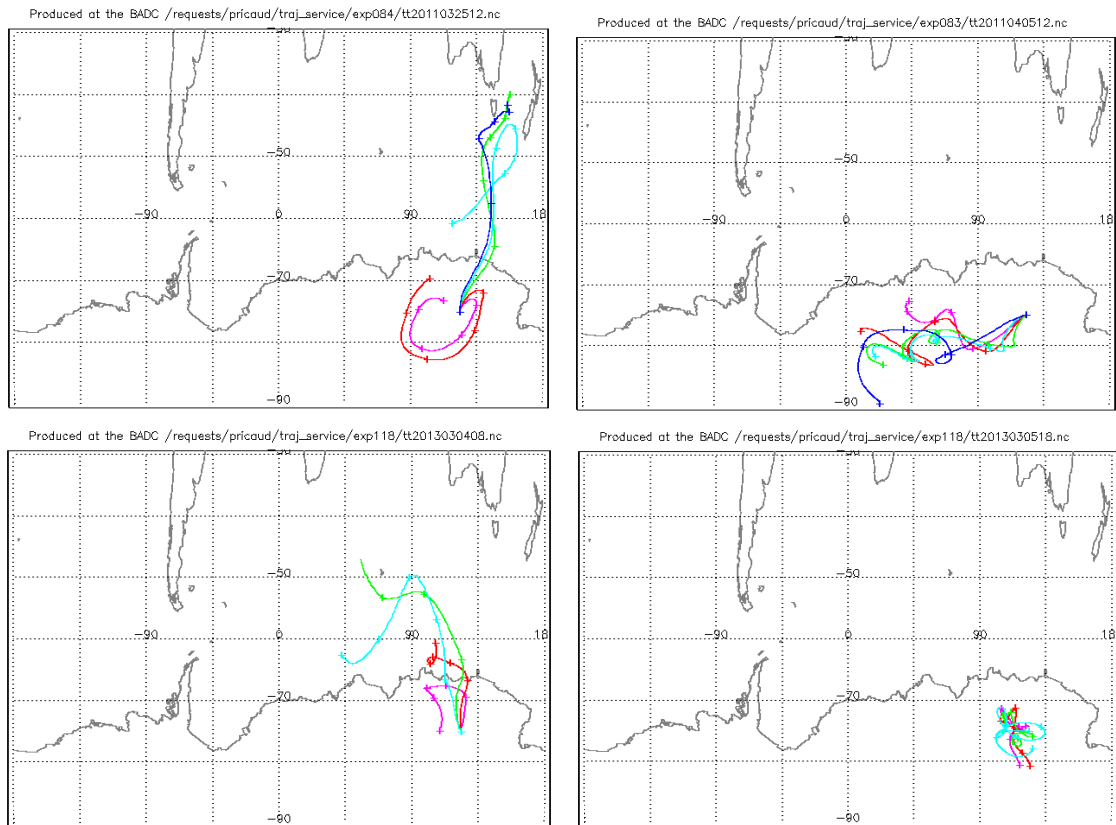
919

920 **Fig. 13:** Vertical distribution of temperature measured by HAMSTRAD (solid line), and
 921 radiosondes (dashed lines) and calculated by ARPEGE (dotted lines) on 4 March 12:00 UTC
 922 (red line) and 18:00 UTC (orange line) and on 5 March 12:00 UTC (blue line) and 18:00 UTC
 923 (green line). Note radiosondes are only available at 12:00 UTC.

924

925

926

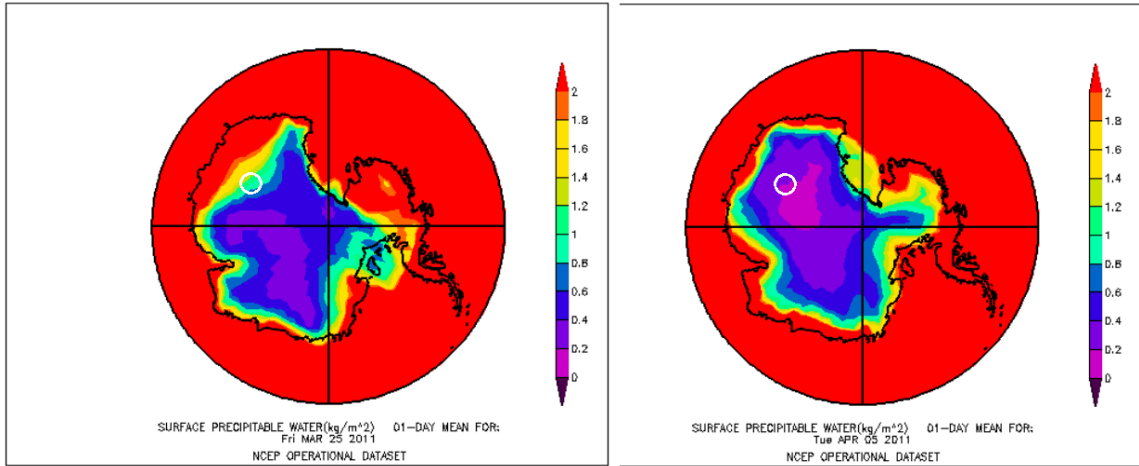


927
928
929
930

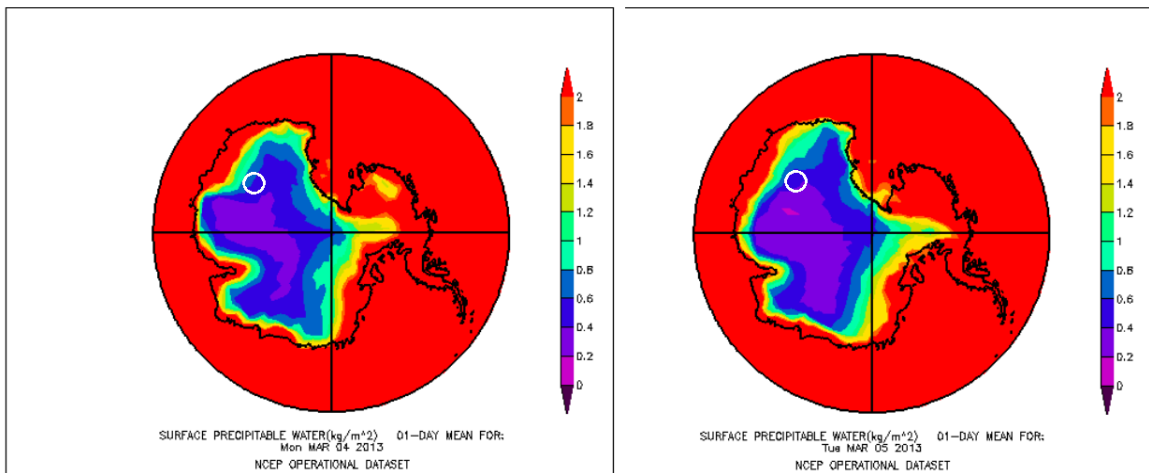
931 **Fig. 14:** (Top) Five-day back-trajectories of air masses originated from Dome C on 25 March
932 2011 at 12:00 UTC (left) and on 5 April 2011 at 12:00 UTC (right) at 650 (pink line), 600 (red
933 line), 500 (green line), 400 (light blue line) and 300 hPa (dark blue line). (Bottom) Same as top
934 but on 4 March 2013 at 08:00 UTC (left) and on 5 March 2013 at 18:00 UTC (right).

935
936

937



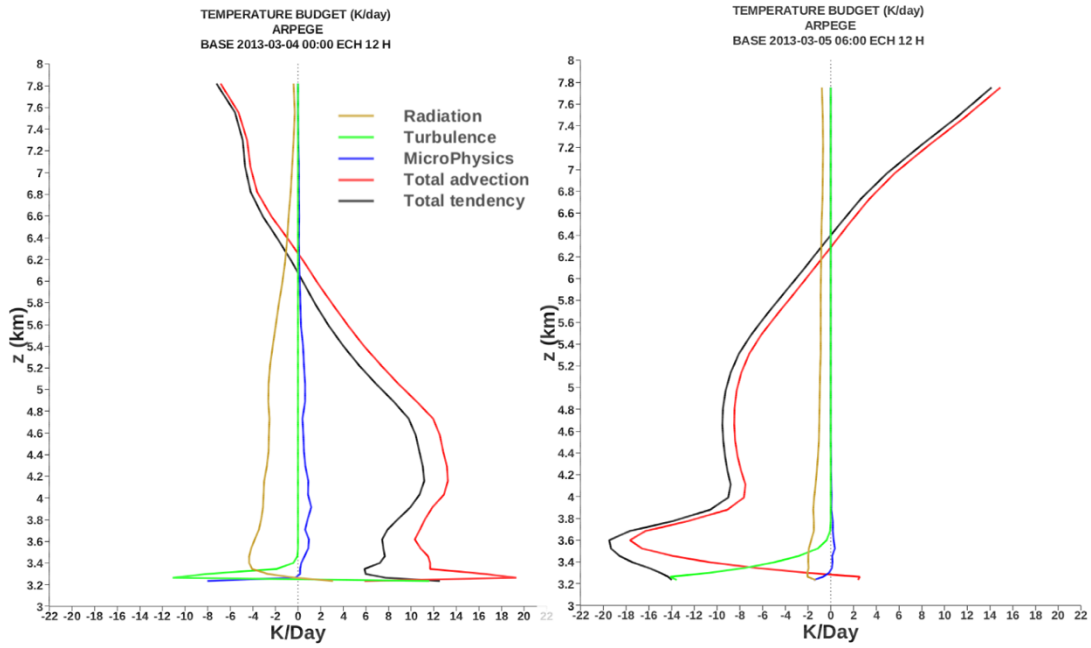
938



939 **Fig. 15:** IWV calculated above the Antarctic continent from the NCEP/NCAR operational
940 analyses on 25 March 2011 (top left), 5 April 2011 (top right), 4 March 2013 (bottom left) and
941 5 March 2013 (bottom right). The white circle represents the position of the Dome C station.

942

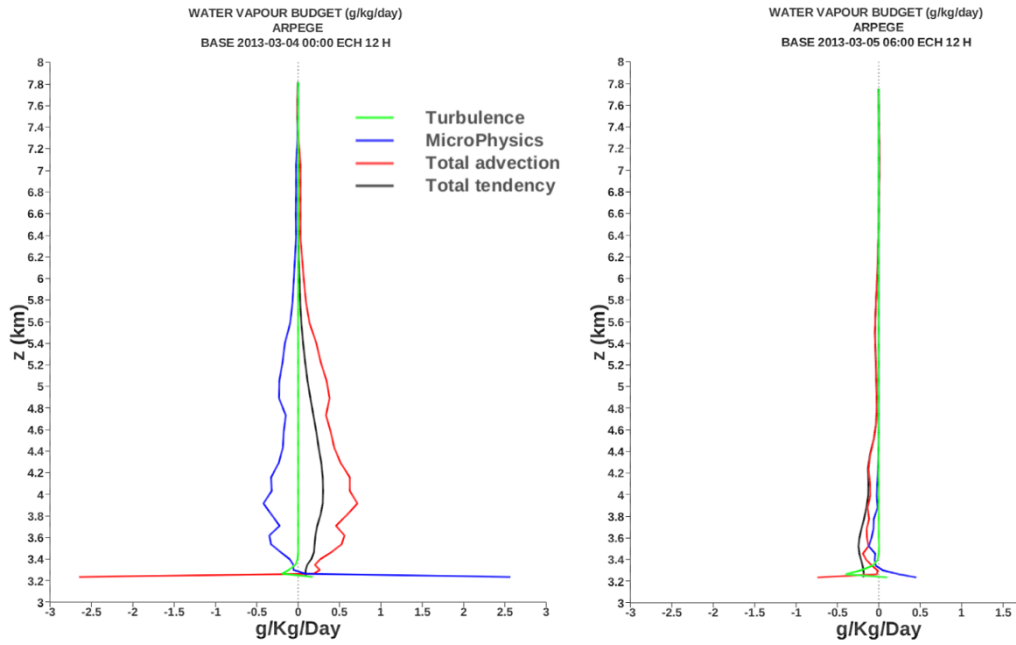
943



944

945 **Fig. 16:** (Left) Temperature budget calculated by ARPEGE on 4 March 2013 over the 12-h
 946 period 00:00-12:00 UTC induced by radiation (brown), turbulence (green), microphysics
 947 (blue), total advection (red) showing the total tendency (black). (Right) Same as Left but on 5
 948 March 2013 over the 12-h period 06:00-18:00 UTC.

949



950

951 **Fig. 17:** (Left) Water vapour budget calculated by ARPEGE on 4 March 2013 over the 12-h
 952 period 00:00-12:00 UTC induced by turbulence (green), microphysics (blue), total advection
 953 (red) showing the total tendency (black). (Right) Same as Left but on 5 March 2013 over the
 954 12-h period 06:00-18:00 UTC.

955

956